



Infinitely many multipulse solitons of different symmetry types in the nonlinear Schrödinger equation with quartic dispersion

Ravindra I. Bandara ^{1,2,*} Andrus Giraldo ^{1,2} Neil G. R. Broderick^{1,3} and Bernd Krauskopf^{1,2}

¹*Dodd-Walls Centre for Photonic and Quantum Technologies, New Zealand*

²*Department of Mathematics, University of Auckland, Auckland 1010, New Zealand*

³*Department of Physics, University of Auckland, Auckland 1010, New Zealand*



(Received 29 March 2021; accepted 1 June 2021; published 21 June 2021)

We show that the generalized nonlinear Schrödinger equation (GNLSE) with quartic dispersion supports infinitely many multipulse solitons for a wide parameter range of the dispersion terms. These solitons exist through the balance between the quartic and quadratic dispersions with the Kerr nonlinearity, and they come in infinite families with different signatures. A traveling wave ansatz, where the optical pulse does not undergo a change in shape while propagating, allows us to transform the GNLSE into a fourth-order nonlinear Hamiltonian ordinary differential equation with two reversibilities. Studying families of connecting orbits with different symmetry properties of this reduced system, connecting equilibria to themselves or to periodic solutions, provides the key to understanding the overall structure of solitons of the GNLSE. Integrating a perturbation of them as solutions of the GNLSE suggests that some of these solitons may be observable experimentally in photonic crystal waveguides over several dispersion lengths.

DOI: [10.1103/PhysRevA.103.063514](https://doi.org/10.1103/PhysRevA.103.063514)

I. INTRODUCTION

Recently, Blanco-Redondo *et al.* experimentally discovered pure quartic solitons (PQS) in a silicon photonic crystal waveguide [1]. Such PQS exist due to a balance between negative quartic dispersion and the Kerr nonlinearity, unlike conventional optical solitons which balance quadratic dispersion and nonlinearity. This balance through the quartic dispersion allows for an unusual scaling of the pulse width with the power, which makes them attractive for short-pulse lasers [1]. Furthermore, these new solitons have decaying oscillating tails. Pure quartic solitons have been the focus of several recent studies, both experimental and theoretical [2–4].

It is well known that the generalized nonlinear Schrödinger equation (GNLSE) can be used to model optical pulse propagation in fibers in a variety of different regimes, including the case of higher-order dispersion. An analytic solution in the presence of both quartic and quadratic dispersion was found by Karlson and Höök [5] in the form of a squared hyperbolic secant pulse shape. It exists in the situation when both the quadratic and the quartic dispersion coefficients β_2 and β_4 are negative. Furthermore, the Karlson and Höök solution family does not possess oscillating decaying tails; thus, it does not describe PQS. Subsequently, Piché *et al.* [6] numerically studied the effect of third-order dispersion together with second- and fourth-order dispersions. With numerical simulations, they found that, when a weak third-order dispersion is introduced, the temporal profile and the peak power of the soliton remain unchanged. Akhmediev *et al.* [7] found

that, when both β_2 and β_4 are negative, solitons have either exponentially decaying tails or oscillating tails, depending on the soliton propagation constant (nonlinear shift of the wave number). Interaction of solitons with oscillating tails was numerically studied by Akhmediev and Buryak [8]. They found that the oscillating tails of a soliton establish a potential barrier between neighboring solitons during their interactions, preventing two adjacent solitons from combining. Furthermore, they investigated the bound states of two or more solitons when the single soliton has oscillating tails [9]. Roy and Biancalana [10] demonstrated that, when both β_2 and β_4 are negative, it is possible to observe solitons in silicon-based slot waveguides. Although there have been many studies of solitons in the presence of both quartic and quadratic dispersions, all these works considered the situation when both β_2 and β_4 are negative. More recently Tam *et al.* [2,4] considered the case when β_4 is negative while β_2 can have either sign. They numerically found that single-hump solitons exist for some positive β_2 values as well. Furthermore, they explained that the decay rate of the solitons decreases as β_2 increases.

In this paper, we perform a detailed analysis of the GNLSE to find solitons of different types (multihump solitons) with different symmetry properties, beyond the one-hump soliton obtained in [4] and for different signs of the quadratic dispersion term. More specifically, we show that the GNLSE supports infinitely many and different types of multihump solitons in the presence of both quartic and quadratic dispersion. Note that the multihump solitons we present here are distinct from bound states of two or more primary solitons that arise, for example, in dispersion-managed optical fibers [11,12]. Taking a dynamical system approach allows us to systematically find and characterize families of solitons with different symmetry properties; this general approach has

*ravindra.bandara@auckland.ac.nz

been successfully applied to other systems, including a widely studied class of the NLSE describing solitary wave formation in inhomogeneous media [13–16] and bright localized structures described by the Lugiato-Lefever equation [17]. To identify infinite families of multihump solitons, we consider the situation when β_4 is negative and show that such solitons exist not only when β_2 is negative. More specifically, we extend the work in [4] and [9] and present the parameter range for which these multihump solitons also exist when β_2 is positive. Moreover, we show that, apart from symmetric and antisymmetric solitons, there also exist nonsymmetric, symmetry-broken solitons, which are distinct from a union of fundamental solitons. For fixed negative β_4 , we determine the parameter intervals of β_2 over which the different types of solitons exist. This is achieved via a traveling wave ansatz that transforms the GNLSE into a fourth-order Hamiltonian ordinary differential equation (ODE) with two reversible symmetries. Solitons of the GNLSE are then identified as homoclinic solutions to the origin of this ODE, which we find and track with state-of-the-art continuation techniques. We discuss a connection of our findings with results obtained, for example, for the Swift-Hohenberg equation [18] and the Lugiato-Lefever equation [17], and demonstrate that the overall bifurcation structure of the GNLSE can be characterized as truncated homoclinic snaking. Moreover, we show that connecting orbits from the origin to periodic orbits (also referred to as EtoP connections) with different symmetry properties organize different infinite families of multihump solitons. The structure of periodic orbits is discussed briefly to show that infinitely many of them create different connections to the origin and, hence, associated families of solitons. Importantly, our results apply to any negative values of the quartic dispersion term via a suitable transformation. Finally, we investigate the evolution of these solitons along a waveguide via the integration of the GNLSE with a split-step Fourier method; here we consider symmetric and nonsymmetric solitons for $\beta_2 = 0$ and also for different signs of β_2 . Our numerical simulations indicate that some of the multihump solitons are only weakly unstable and may propagate effectively unchanged over many dispersion lengths; hence, they might be observable in careful experiment with currently available waveguides.

The paper is structured as follows. In Sec. II, we introduce the GNLSE, and show how it can be transformed into an ODE; we then discuss the special mathematical properties of this ODE, present its local bifurcation analysis, and also discuss the role of its homoclinic solutions as solitons of the GNLSE. In Sec. III, we set up suitable boundary value problems to find and then continue homoclinic solutions, periodic solutions, and EtoP connections. In Sec. IV, we present, one-by-one, families of homoclinic solutions of different symmetry types, show over which β_2 range they exist, and discuss their connection with homoclinic snaking. Section V then shows that the respective homoclinic solutions occur along parabolas in different parameter planes. In Sec. VI we show that there are infinitely many periodic orbits that create families of connecting orbits and, hence, a menagerie of solitons with different signatures. In Sec. VII, we present some simulations of the GNLSE that demonstrate that, while only the single-pulse primary soliton is stable, certain multihump solitons are only

weakly unstable and, thus, may be observable in an experimental setting. Finally, a discussion of the results and an outlook to future research are presented in Sec. VIII.

II. MATHEMATICAL ANALYSIS

Pulse propagation along an optical fiber under the influence of quadratic dispersion, quartic dispersion, and the Kerr nonlinearity is governed by the GNLSE [19]

$$\frac{\partial A}{\partial z} = i\gamma|A|^2A - i\frac{\beta_2}{2}\frac{\partial^2 A}{\partial t^2} + i\frac{\beta_4}{24}\frac{\partial^4 A}{\partial t^4}. \quad (1)$$

Here, $A(z, t)$ is the slowly varying complex pulse envelope, z is the propagation distance, t is the time in a comoving frame of the pulse, γ is the coefficient of the nonlinearity, and β_2 and β_4 are the quadratic and quartic dispersion coefficients, respectively. In order to focus on the essential interactions between dispersion and nonlinearity that drive soliton formation, Eq. (1) does not include losses and higher-order terms such as the Raman effect.

We note that the rescaling transformations

$$U = \sqrt{\frac{|\beta_4|\gamma}{6\beta_2^2}}A, \quad x = \frac{6\beta_2^2}{|\beta_4|}z, \quad \tau = \sqrt{\frac{12|\beta_2|}{|\beta_4|}}t,$$

which are defined only for $\beta_2 \neq 0$ and $\beta_4 \neq 0$, reduce Eq. (1) to the parameter-free form

$$\frac{\partial U}{\partial x} = i|U|^2U - \text{sign}(\beta_2)i\frac{\partial^2 U}{\partial \tau^2} + \text{sign}(\beta_4)i\frac{\partial^4 U}{\partial \tau^4}. \quad (2)$$

Clearly, each open quadrant of the (β_2, β_4) plane corresponds to fixed signs of β_2 and β_4 and, hence, a unique reduced PDE; for ease of reference, we refer to these four different cases as

- (a) $\beta_2 > 0, \beta_4 > 0$; (b) $\beta_2 < 0, \beta_4 > 0$;
- (c) $\beta_2 > 0, \beta_4 < 0$; (d) $\beta_2 < 0, \beta_4 < 0$.

In particular, Akhmediev *et al.* [7] considered the corresponding reduced PDE in quadrant (d); thus, they considered the situation when both β_2 and β_4 are negative. Indeed, the above transformations are undefined when $\beta_2 = 0$ or $\beta_4 = 0$, and there is no continuous transition between different signs of β_2 and β_4 . Therefore, none of the reduced PDEs are able to describe the case of PQS. For the purpose of this paper, we are interested in the transition between $\beta_2 < 0, \beta_2 = 0$ (PQS), and $\beta_2 > 0$. Thus, we consider the original GNLSE without reducing the parameters first. We stress the generality of our results because they can be mapped to any specific parameter region by the transformations for given signs of β_2 and β_4 .

When solving the GNLSE one looks for solutions, where the pulse is stationary and does not change with propagation distance. We study here such traveling wave solutions of the form

$$A(z, t) = u(t)e^{i\mu z}, \quad (3)$$

where $u(t)$ is the temporal profile of the pulse and μ is the soliton propagation constant (nonlinear shift of the wave number) [7]. Note that the intensity of such solutions, $|A(t)|^2 = u(t)^2$, is unchanged during propagation. After substituting

Eq. (3) into (1) we obtain the fourth-order nonlinear ODE

$$\frac{\beta_4}{24} \frac{d^4 u}{dt^4} - \frac{\beta_2}{2} \frac{d^2 u}{dt^2} - \mu u + \gamma u^3 = 0. \quad (4)$$

By introducing the new variables $u_1, u_2, u_3,$ and u_4 such that $\mathbf{u} = (u_1, u_2, u_3, u_4) = (u, \frac{du}{dt}, \frac{d^2 u}{dt^2}, \frac{d^3 u}{dt^3})$, Eq. (4) can be written as the system of four first-order ODEs

$$\frac{d\mathbf{u}}{dt} = f(\mathbf{u}, \zeta) = \begin{pmatrix} u_2 \\ u_3 \\ u_4 \\ \frac{24}{\beta_4} \left(\frac{\beta_2}{2} u_3 + \mu u_1 - \gamma u_1^3 \right) \end{pmatrix}, \quad (5)$$

where $\zeta = (\beta_2, \beta_4, \gamma, \mu) \in \mathbb{R}^4$. Note that system (5) is reversible [20] under the transformations

$$R_1 : (u_1, u_2, u_3, u_4) \rightarrow (u_1, -u_2, u_3, -u_4) \text{ and} \\ R_2 : (u_1, u_2, u_3, u_4) \rightarrow (-u_1, u_2, -u_3, u_4).$$

This means that if $\mathbf{u}(t)$ is a solution, then both $R_1(\mathbf{u}(-t))$ and $R_2(\mathbf{u}(-t))$ are also solutions of system (5). Throughout the paper, we refer to $R_1(\mathbf{u}(-t))$ and $R_2(\mathbf{u}(-t))$ as the R_1 and R_2 counterpart of $\mathbf{u}(t)$, respectively. Furthermore, $S = R_1 \circ R_2 = R_2 \circ R_1$ is the state-space symmetry

$$S : (u_1, u_2, u_3, u_4) \rightarrow (-u_1, -u_2, -u_3, -u_4)$$

of system (5), which is point reflection in the origin $\mathbf{0}$. The set of points that are left invariant under R_1 or R_2 are known as symmetric or reversibility sections of system (5); they are

$$\Sigma_1 = \{\mathbf{u} \in \mathbb{R}^4 : u_2 = u_4 = 0\} \text{ and} \\ \Sigma_2 = \{\mathbf{u} \in \mathbb{R}^4 : u_1 = u_3 = 0\},$$

respectively. Note that the origin $\mathbf{0}$ is the only point that belongs to both Σ_1 and Σ_2 , that is, it is the only point that is invariant under S . A solution trajectory $\mathbf{u}(t)$ of system (4) is called *symmetric* if it satisfies either $R_1(\mathbf{u}(-t)) = \mathbf{u}(t)$ or $R_2(\mathbf{u}(-t)) = \mathbf{u}(t)$. One can show that if $\mathbf{u}(t)$ is a symmetric solution, then there exists a time $t^* \in \mathbb{R}$ such that $\mathbf{u}(t^*) \in \Sigma_1$ or $\mathbf{u}(t^*) \in \Sigma_2$, that is, $\mathbf{u}(t)$ intersects Σ_1 or Σ_2 . To distinguish the invariance between the two reversibility conditions R_1 and R_2 , we refer to a solution that is only invariant under R_1 as R_1 -symmetric solutions of system (5), and similarly define R_2 -symmetric solutions. Furthermore, if a solution is invariant under both R_1 and R_2 , then we refer to it as R^* symmetric. Notice that if a solution is R^* symmetric, then it is invariant under S ; however, invariance under S does not necessarily imply R^* symmetry. Lastly, a solution that is neither invariant under R_1 nor R_2 is referred to as nonsymmetric.

System (5) can be transformed into the form of a Hamiltonian system by the change of coordinates

$$\mathbf{p} = (p_1, p_2) = (u_2, u_4), \\ \mathbf{q} = (q_1, q_2) = \left(\frac{-12\beta_2}{\beta_4} u_1 + u_3, u_1 \right),$$

where \mathbf{p} and \mathbf{q} are the generalized position and momentum coordinates. With this transformation, system (5) can be written

as

$$\begin{pmatrix} \frac{dq_1}{dt} \\ \frac{dq_2}{dt} \\ \frac{dp_1}{dt} \\ \frac{dp_2}{dt} \end{pmatrix} = \begin{pmatrix} \frac{-12\beta_2}{\beta_4} p_1 + p_2 \\ p_1 \\ q_1 + \frac{12\beta_2}{\beta_4} q_2 \\ \frac{24}{\beta_4} \left[\frac{\beta_2}{2} \left(q_1 + \frac{12\beta_2}{\beta_4} q_2 \right) + \mu q_2 - \gamma q_2^3 \right] \end{pmatrix}, \quad (6)$$

which satisfies the well-known Hamiltonian equations [20]

$$\frac{d\mathbf{q}}{dt} = \frac{\partial \hat{H}}{\partial \mathbf{p}}, \quad \frac{d\mathbf{p}}{dt} = -\frac{\partial \hat{H}}{\partial \mathbf{q}}. \quad (7)$$

Here the conserved quantity or energy is

$$\hat{H}(\mathbf{p}, \mathbf{q}) = p_1 p_2 - \frac{6\beta_2}{\beta_4} p_1^2 - \frac{1}{2} \left(q_1 + \frac{12\beta_2}{\beta_4} q_2 \right)^2 \\ + \left(\frac{6\gamma q_2^4 - 12\mu q_2^2}{\beta_4} \right), \quad (8)$$

as obtained from system (6) by integration with respect to \mathbf{p} and \mathbf{q} . This expression can be written in original coordinates as

$$H(\mathbf{u}) = u_2 u_4 - \frac{1}{2} u_3^2 - \left(\frac{6\beta_2 u_2^2 - 6\gamma u_1^4 + 12\mu u_1^2}{\beta_4} \right), \quad (9)$$

and it is a conserved quantity along solution trajectories of system (5). We remark that one can also derive Eq. (9) by using the general expression for fourth-order reversible systems provided in [21]. Notice that, if a solution trajectory converges backward or forward in time to an equilibrium \mathbf{u}_0 of system (5) with energy $H(\mathbf{u}_0)$, then the solution trajectory has energy $H(\mathbf{u}_0)$ for all times.

We now focus our attention on the equilibria of system (5). The origin $\mathbf{0} = (0, 0, 0, 0)$ is an equilibrium for any parameter value. It undergoes a pitchfork bifurcation at $\mu = 0$, which creates two equilibria $\mathbf{E}_\pm = (\pm\sqrt{\mu/\gamma}, 0, 0, 0)$ for $\mu\gamma > 0$. These are the only equilibria of system (5). Note that $\mathbf{0} \in \Sigma_1 \cap \Sigma_2$, while \mathbf{E}_\pm lie only in Σ_1 . Hence, all equilibria are symmetric: $\mathbf{0}$ is invariant under both R_1 and R_2 , and \mathbf{E}_\pm are invariant under R_1 only. Note from Eq. (9) that, for any choice of the parameters, $\mathbf{0}$ always lies in the zero-energy level. This is not the case for the other two equilibria \mathbf{E}_\pm for which $H(\mathbf{E}_\pm) = -\frac{6\mu^2}{\gamma\beta_4}$. Hence, $H(\mathbf{E}_\pm) \neq 0$ whenever $\mu \neq 0$ (and $\beta_4, \gamma \neq 0$), so that the equilibria $\mathbf{0}$ and \mathbf{E}_\pm do not lie in the same energy level. Thus, there cannot be a connecting trajectory between them.

We now focus our attention on *homoclinic solutions*, which are trajectories of system (5) that converge to the same equilibrium both forward and backward in time. Homoclinic solutions are sought because they correspond to solitons of the GNLSE. Since the solitons of the GNLSE converge to 0, both forward and backward in time, we only consider homoclinic solutions to $\mathbf{0}$ as it is the only equilibrium with $u = u_1 = 0$.

Homoclinic solutions in fourth-order, reversible, and Hamiltonian systems have been studied, for example, in [20–26]. In particular, results on four-dimensional reversible systems have been developed and applied in the analysis of a system that describes the dynamics of an elastic strut [20,21,24,25]. It is the case that symmetric homoclinic

solutions in fourth-order reversible systems persist when a suitable parameter is changed [21–23]. This is true for both reversible and nonreversible Hamiltonian systems. It has also been proved that each symmetric homoclinic solution in a reversible system is accompanied, for fixed parameter values, by a one-parameter family of periodic solutions with minimal period T_0 . As the period grows to infinity, that is $T_0 \rightarrow \infty$, periodic solutions accumulate on a symmetric homoclinic solution. The periodic solutions of these families lie in different Hamiltonian energy levels, and some of them lie in the energy level with $H = 0$. As opposed to the symmetric case, nonsymmetric homoclinic solutions in reversible systems do not persist as a suitable parameter is changed; however, they persist in systems that are both reversible and Hamiltonian [21,27] as is the case for system (5). It is a special property of systems that are both reversible and Hamiltonian that homoclinic solutions persist as codimension-zero phenomena. It has been proven in [25] that a transition of the equilibrium from a real saddle (spectrum with only real eigenvalues) to a saddle focus (spectrum with only complex-conjugate eigenvalues), as a parameter is changed, is an organizing center for the creation of infinitely many symmetric homoclinic solutions, provided the following conditions are satisfied:

- (1) the ODE is fourth-order, reversible and Hamiltonian,
- (2) there exists a symmetric homoclinic solution at the moment of the transition of the equilibrium.

One refers to this transition as the Belyakov-Devaney (BD) bifurcation [17,21,22,28]. To see whether the second condition is satisfied for system (5), we first focus our attention on the eigenvalues of its equilibria in different parameter regimes. The eigenvalues of the linearization around a symmetric equilibrium of a reversible system have generically one of the following forms [20]:

- (I) two eigenvalues are $\pm\lambda_1$ and the other two are $\pm\lambda_2$, where $\lambda_1, \lambda_2 \in \mathbb{R}$;
- (II) two eigenvalues are $\pm\lambda$ and the other two are $\pm\lambda^*$, where $\lambda \in \mathbb{C}$ with $\text{Re}(\lambda) \neq 0$ and $\text{Im}(\lambda) \neq 0$;
- (III) two eigenvalues are $\pm i\lambda_1$ and the other two are $\pm i\lambda_2$, where $\lambda_1, \lambda_2 \in \mathbb{R}$;
- (IV) two eigenvalues are $\pm\lambda_1$ and the other two are $\pm i\lambda_2$, where $\lambda_1, \lambda_2 \in \mathbb{R}$.

For system (5), one can obtain an analytical expression for the eigenvalues of the linearization around $\mathbf{0}$ and \mathbf{E}_\pm . The eigenvalues of $\mathbf{0}$ are given by [4,21]

$$\lambda_{\mathbf{0}}^2 = \frac{6\beta_2}{\beta_4} \left(1 \pm \sqrt{1 + \frac{2\beta_4}{3\beta_2^2}\mu} \right), \quad (10)$$

while the eigenvalues of \mathbf{E}_\pm are given by

$$\lambda_{\mathbf{E}_\pm}^2 = \frac{6\beta_2}{\beta_4} \left(1 \pm \sqrt{1 - \frac{4\beta_4}{3\beta_2^2}\mu} \right). \quad (11)$$

Since we are interested in homoclinic solutions to $\mathbf{0}$, we focus our attention on Eq. (10). Notice that the expression inside the square root defines a parabola in the (β_2, μ) plane that separates the different cases of the spectrum of the equilibrium $\mathbf{0}$. This parabola is shown in Fig. 1(a) as a purple curve that separates the (β_2, μ) plane into three regions, where the

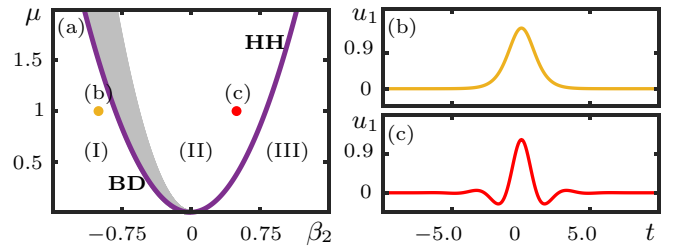


FIG. 1. (a) Shows the bifurcation diagram in the (β_2, μ) plane for $\beta_4 = -1$ and $\gamma = 1$. The purple parabola denotes the boundary between the equilibrium $\mathbf{0}$ having real and complex eigenvalues, given by BD and HH bifurcation; in the gray shaded region close to the purple parabola, infinitely many symmetric homoclinic solutions are expected to exist. (b), (c) Show the temporal traces of the primary homoclinic solution of system (5) for $(\beta_2, \beta_4, \gamma, \mu) = (-1, -1, 1, 1)$ and $(\beta_2, \beta_4, \gamma, \mu) = (0.4, -1, 1, 1)$, at the yellow and orange dots in (a), respectively.

eigenvalues of $\mathbf{0}$ are of the form (I), (II), and (III), respectively. Note that $\mathbf{0}$ is a real saddle in region (I) and a saddle-focus in region (II). Due to the real eigenvalues of $\mathbf{0}$, homoclinic solutions in region (I) must have nonoscillatory exponentially decaying tails. In contrast, homoclinic solutions in region (II) must have oscillatory decaying tails because the eigenvalues of $\mathbf{0}$ are complex conjugates. In the following sections up to Sec. V, we present our results on the existence of homoclinic solutions for the horizontal line $\mu = 1$ in the (β_2, μ) plane. This choice of μ value does not restrict the generality of our results as we will show in Sec. V; indeed, our results extend throughout the upper half of the (β_2, μ) plane, that is, when $\mu > 0$. Figures 1(b) and 1(c) show two homoclinic solutions along this horizontal line for two distinct β_2 values in region (I) and (II), respectively. The homoclinic solution in Fig. 1(b) has nonoscillating exponentially decaying tails as it belongs to region (I). Furthermore, this homoclinic solution persists until β_2 reaches the right-hand side of the parabola in Fig. 1(a), that is, at the boundary between regions (II) and (III), which correspond to a Hamiltonian-Hopf (HH) bifurcation [28,29]. In Fig. 1(c), we show what this homoclinic solution looks like at $\beta_2 = 0.4$ where it has oscillating tails. In particular, this homoclinic solution is R_1 symmetric and we refer to it as the primary homoclinic solution; its corresponding soliton is the one Tam *et al.* considered in [2]. Note that the homoclinic solution in Fig. 1(c) has oscillatory decaying tails but the oscillations damp out very quickly. The oscillations in the tails of these homoclinic solutions increase when moving horizontally towards the bifurcation HH. Because the primary homoclinic solution exists at the transition between regions (I) and (II), the conditions for a BD bifurcation are satisfied and infinitely many homoclinic solutions must exist in the indicated gray shaded region near the branch BD in Fig. 1(a) [25].

III. NUMERICAL IDENTIFICATION AND CONTINUATION OF HOMOCLINIC SOLUTIONS

The task is now to find and identify a representative number of symmetric and nonsymmetric homoclinic solutions of system (5). To this end, we make use of continuation al-

gorithms for two-point boundary value problems (2PBVP), implemented in the software package AUTO-07P [30] and its extension HOMCONT [31]. In the 2PBVP formulation, time is rescaled to the interval $[0,1]$. Thus, the integration time is treated as a free parameter that multiplies the right-hand side of system (4), that is,

$$\frac{d\mathbf{v}}{dt} = Tf(\mathbf{v}, \zeta). \quad (12)$$

Note that we always assume that $T > 0$. Suitable boundary conditions are imposed at the starting point $\mathbf{v}(0)$ and the end point $\mathbf{v}(1)$ of the solution segment [32]. For the continuation of a homoclinic solution, we use projection boundary conditions that place $\mathbf{v}(0)$ in the unstable eigenspace $E_u(\mathbf{0})$ of the equilibrium $\mathbf{0}$, and $\mathbf{v}(1)$ in one of the reversibility sections Σ_1 or Σ_2 . In this way, we take advantage of the reversibility of system (5) to compute only half of a symmetric homoclinic solution $\mathbf{v}(t)$. Convergence forward in time to the stable eigenspace $E_s(\mathbf{0})$ is guaranteed by the corresponding reversibility conditions, and the remaining part of the homoclinic solution is obtained by applying $R_1(\mathbf{v}(-t))$ or $R_2(\mathbf{v}(-t))$. Notice that this formulation is only able to continue symmetric homoclinic solutions since an intersection with a reversibility section is required.

For the case of nonsymmetric homoclinic solutions we formulate a 2PBVP of the entire homoclinic solution. AUTO-07P is a general-purpose continuation package designed for generic vector fields, and particular considerations have to be taken when continuing homoclinic and periodic solutions in reversible and Hamiltonian systems [33]. To deal with the fact that homoclinic solutions generically persist when a single parameter is varied, we follow [33] and introduce the gradient of the conserved quantity H as a perturbation of the vector field equations

$$\frac{d\mathbf{v}}{dt} = Tf(\mathbf{v}, \zeta) + \delta \nabla H, \quad (13)$$

where δ is an additional continuation parameter. We then impose the boundary conditions that $\mathbf{v}(0)$ lies in $E_u(\mathbf{0})$ and $\mathbf{v}(1)$ lies in $E_s(\mathbf{0})$. We continue the solution of the overall 2PBVP in one of the parameters while allowing δ and T to vary. In this setup, the new parameter δ is free but remains extremely close to zero during continuation [33–35]. Note that the 2PBVP formulation of the entire homoclinic solution can be used to continue symmetric homoclinic solutions as well.

To find the first homoclinic solution, we make use of a numerical implementation of Lin's method [36], where we consider two orbit segments $\mathbf{v}_a(t)$, $\mathbf{v}_b(t)$ and a suitable three-dimensional hyperplane Σ . Here, $\mathbf{v}_a(0)$ and $\mathbf{v}_b(1)$ lie in $E_u(\mathbf{0})$ and $E_s(\mathbf{0})$, respectively, and $\mathbf{v}_a(1)$ and $\mathbf{v}_b(0)$ both lie in Σ . Then, the signed difference (called the Lin gap) between $\mathbf{v}_a(1)$ and $\mathbf{v}_b(0)$, along a fixed one-dimensional direction, provides a well-defined test function whose zeros correspond to homoclinic solutions of system (5) (see [36]). Once a zero is found, the associated homoclinic solution can be followed in system parameters with the previously constructed 2PBVP formulations. Lin's method allows us to compute multihump homoclinic solutions of different types. We remark that the AUTO DEMO REV [30], for the GNLSE as considered in [37],

contains a setup to continue the basic homoclinic solutions. However, we are interested in many different types of homoclinic solutions that cannot be computed from the demo, and they are all identified here with Lin's method.

Connections between the equilibrium $\mathbf{0}$ and periodic solutions, which we refer to as EtoP connections, are organizing centers for the existence of homoclinic solutions under mild conditions [38,39]; hence, they are an important object to consider when studying homoclinic solutions. To compute EtoP connections, we have to find first periodic solutions of system (5) that support a connection to $\mathbf{0}$. In reversible and Hamiltonian systems, periodic solutions are not isolated in phase space for fixed parameter values [33]. To be able to compute and continue them, we consider the perturbed system (13) and use the 2PBVP formulation for periodic solutions [32]. For the initial data of the formulation, we use homoclinic solutions previously constructed with the 2PBVP above, as they are good initial approximations of periodic solutions of high period. Performing a continuation step in δ and T allows us to find the family of periodic solutions for fixed parameter values, while δ again remains practically 0. These solution families form two-dimensional surfaces in phase space where each periodic solution lies in a particular energy level. Among these solution families, we focus on saddle periodic solutions in the zero-energy level because they are the only periodic solutions that can have connections with $\mathbf{0}$.

To find connections from $\mathbf{0}$ to a saddle periodic solution we can follow the approach that we used to find homoclinic solutions to $\mathbf{0}$. This requires one to compute first the Floquet multipliers and Floquet bundles of the periodic solution, as they contain the linear information of the flow near the periodic solution. Saddle periodic solutions of system (5) have one stable (inside the unit circle) and one unstable (outside of the unit circle) Floquet multipliers with associated stable and unstable Floquet bundles, respectively. The stable (unstable) bundle consists of the directions in phase space, along which solutions converge forward (backward) in time to the periodic solution. Finally, the other two Floquet multipliers of a saddle periodic solution in system (5) are always equal to one. Associated to them, there are two Floquet bundles: one that is pointing in the direction of the flow along the periodic solution, called the trivial bundle, and another one tangent to the surface of the periodic solutions in phase space.

We compute the Floquet multipliers and their corresponding bundles with a homotopy step for a suitable 2PBVP formulation; see [40] for more details. Note that any connection that converges backward in time to $\mathbf{0}$ and forward in time to an R_1 -symmetric (R_2 -symmetric) periodic solution has an R_1 counterpart (R_2 counterpart) that converges backward in time to the same periodic solution and forward in time to $\mathbf{0}$. As we are interested in periodic solutions that are R_1 symmetric or R_2 symmetric, we make use of this fact to set up Lin's method by using the unstable eigenspace $E_u(\mathbf{0})$ of $\mathbf{0}$ and the stable bundle of the periodic solution. That is, we consider two orbit segments $\mathbf{v}_a(t)$, $\mathbf{v}_b(t)$ and a suitable three-dimensional hyperplane Σ , such that $\mathbf{v}_a(0)$ and $\mathbf{v}_b(1)$ lie in $E_u(\mathbf{0})$ and the stable Floquet bundle of the saddle periodic solution, respectively, and $\mathbf{v}_a(1)$ and $\mathbf{v}_b(0)$ lie in Σ . The zeros

of the corresponding Lin gap correspond to EtoP connections that converge backwards in time to $\mathbf{0}$ and forward in time to the periodic solution.

IV. HOMOCLINIC FAMILIES OF DIFFERENT TYPES

Computing EtoP connections between $\mathbf{0}$ and saddle periodic solutions in the zero-energy level is a good starting point for understanding how different homoclinic solutions are organized. Since system (5) is reversible, existence of a connection from $\mathbf{0}$ to a *symmetric* saddle periodic solution guarantees a return connection from the periodic solutions to $\mathbf{0}$ as well. This return connection corresponds to the R_1 or R_2 counterpart of the EtoP connection, depending on the symmetry of the periodic solution. The existence of a connection from $\mathbf{0}$ to a periodic solution and a connection back from the periodic solution to $\mathbf{0}$ is known as a heteroclinic cycle. Existence of these heteroclinic cycles, and their persistence under parameter variation (transversality), generate a mechanism for the existence of homoclinic solutions that go around the periodic solution multiple times, as a consequence of the λ lemma [38,41]. Thus, it is possible to find homoclinic solutions that

- (a) follow closely an EtoP connection from $\mathbf{0}$ to the periodic solution,
- (b) then loop n times close to the periodic solution, and
- (c) follow closely an EtoP connection from the periodic solution back to $\mathbf{0}$.

The different combinations of EtoP connections generate cycles with different symmetry properties that organize specific homoclinic solution families in parameter space. Some of these families are organized by EtoP connections to an R^* -symmetric periodic solution, and others by EtoP connections to an R_1 -symmetric periodic solution. The corresponding solitons associated with these homoclinic families are distinct from bound states of two or more primary solitons since the spacing of the maxima is fixed and different from the location of the zeros of the oscillating tails. In what follows, we study different families of such homoclinic solutions. We show bifurcation diagrams in β_2 of these families to illustrate how they persist and coalesce due to the existence of different underlying EtoP connections.

A. Homoclinic solutions associated with R^* -symmetric periodic solution

Heteroclinic cycles from $\mathbf{0}$ to a R^* -symmetric periodic solution organize two main families of homoclinic solutions: the R_1 - and R_2 -symmetric families. Furthermore, these families also organize nonsymmetric homoclinic solutions that arise when the corresponding reversibility condition is broken.

1. R_1 -symmetric homoclinic solutions

Figure 2 illustrates a family of solutions associated with an R^* -symmetric periodic solution Γ_* along with their bifurcation diagram. Figures 2(a1) and 2(a2) show two distinct EtoP connections from $\mathbf{0}$ to Γ_* for $(\beta_2, \beta_4, \gamma, \mu) = (0.4, -1, 1, 1)$. Both these EtoP connections converge backward in time to $\mathbf{0}$ and forward in time to Γ_* ; however, these connections are not related by symmetry as their temporal profiles are

different and cannot be mapped to each other by any of the reversibilities or the spatial-temporal symmetry. In particular, the EtoP connection shown in Fig. 2(a1) makes a small negative excursion in u_1 and then has a transient for positive u_1 before converging to Γ_* after $t \approx 0$; in Fig. 2(a2), on the other hand, it makes two oscillations for positive u_1 before it traces Γ_* from $t \approx 4$. Since Γ_* is R^* symmetric, there exist the R_1 and R_2 counterparts of the EtoP connections, which are reflections in t and rotations by 180° of Fig. 2(a), respectively. The different combinations of these EtoP connections create different heteroclinic cycles that organize different types of homoclinic solutions.

We first consider the heteroclinic cycle that is formed by the EtoP connection shown in Fig. 2(a1) and its corresponding R_1 counterpart. The temporal profiles of the u_1 component of two homoclinic solutions organized by this cycle are shown in Figs. 2(b1) and 2(c1). The homoclinic solution in Fig. 2(b1) can be thought of as a concatenation of first part of the EtoP connection in Fig. 2(a1) up to its second maximum with its R_1 -symmetric counterpart. Similarly, the homoclinic solution in Fig. 2(b2) is associated with the EtoP cycle formed by the connection in Fig. 2(a2) and its R_1 -symmetric counterpart. Two further homoclinic solutions are shown in Figs. 2(c1) and 2(c2); they are derived from the EtoP connections in Figs. 2(a1) and 2(a2) in the same way but for one further half-turn around Γ_* .

This type of homoclinic solution exists for any number of humps, including those with three and four shown in Figs. 2(b1)–2(c2). They all exhibit oscillating tails with oscillations that damp out quickly, and these homoclinic solutions follow the respective EtoP connection in Fig. 2(a) to intersect Σ_1 transversally at $t = 0$ where they start following the R_1 -symmetric counterpart. Hence, they are R_1 -symmetric homoclinic solutions. Note that the R_2 counterparts of the R_1 -symmetric homoclinic solution also exist. However, we do not show them here because, on the level of this figure, they correspond to reflections of u_1 in the t axis so that maxima become minima and vice versa.

Figure 2(d) shows the bifurcation diagram of the EtoP connections and R_1 -symmetric homoclinic solutions in the $(\beta_2, \|u_1\|^2)$ plane. Here, the dotted vertical lines bound the interval $(-0.8164, 0.8164)$, where the equilibrium $\mathbf{0}$ is a saddle focus; hence, this interval represents the β_2 values, between BD and HH, where homoclinic solutions with oscillating tails exist; the shaded gray region represents the region close to the parabola in Fig. 1(a). The EtoP connections in Fig. 1(a) lie on a single curve with two branches that meet at a fold at $\beta_2 \approx 0.5753$; the EtoP connections in Figs. 2(a1) and 2(a2) are from the upper and the lower branches of this curve, respectively. As the EtoP connections have an infinite L_2 norm, we represent them in Fig. 2(d) with a finite norm by truncating the connection after 10 oscillations near the periodic solution. The parameter value where they fold is the moment where two R_1 -symmetric EtoP cycles coalesce; they no longer exist beyond that value. Hence, pairs of R_1 -symmetric EtoP cycles exist for $\beta_2 \in (-0.8164, 0.5753)$ and they come together at $\beta_2 \approx 0.5753$. This has far-reaching consequences for the organization of the two families of R_1 -symmetric homoclinic solutions associated with Γ_* , as is illustrated in Fig. 2(d). All R_1 -symmetric homoclinic solutions also lie on

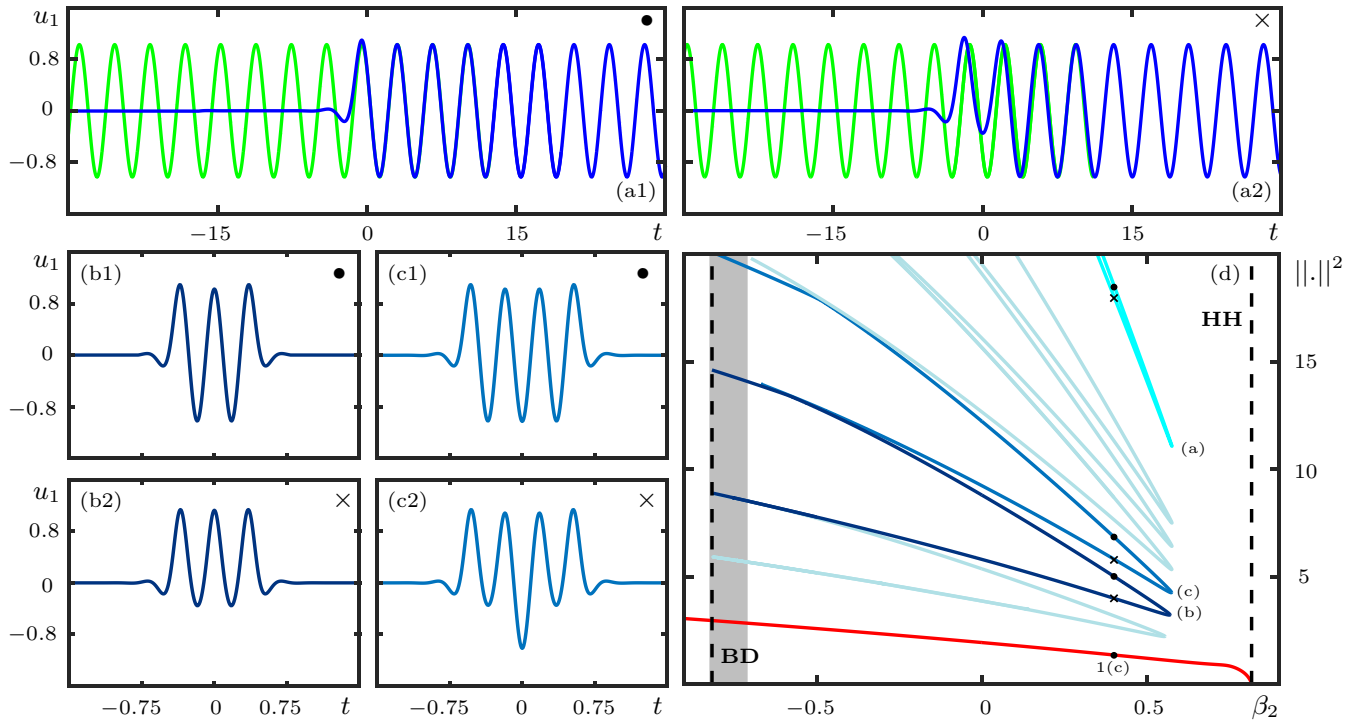


FIG. 2. Family of R_1 -symmetric homoclinic solutions associated with R^* -symmetric periodic solution. (a1), (a2) Show two EtoP connections (blue curves, starting at 0) between $\mathbf{0}$ and a periodic solution Γ_* (green oscillating curve) that is invariant under both R_1 and R_2 . (b1), (c1) and (b2), (c2) Show temporal traces of R_1 -symmetric homoclinic solutions, associated with the connections shown in (a1) and (a2), respectively. (d) Shows the bifurcation diagram in β_2 of the EtoP connections (cyan, top right curve) and R_1 -symmetric homoclinic solutions, where solutions are represented by the square of the L_2 norm of their u_1 component, and each R_1 -symmetric homoclinic curve represents a family of homoclinic solutions that have the same number of humps. Notice that the colors of homoclinic solutions in (b) and (c) and their corresponding bifurcation curves in (d) are the same. The black dot on the bottom curve (red) corresponds to the primary homoclinic solution shown in Fig. 1(c); the black dot and black cross on other bifurcation curves correspond to the solutions shown in (b1),(c1) and (b2),(c2), respectively. The black dashed lines delimit the parameter interval where $\mathbf{0}$ has complex eigenvalues with nonzero real parts: the one on the left indicates the BD bifurcation, and the one on the right the HH bifurcation. The shaded gray region represents the region close to the parabola in Fig. 1(a). Also shown are the bifurcation curves (light blue, not labeled) of the R_1 -symmetric homoclinic solutions that have two, five, six, and seven humps. The bifurcation curves in (d) are for $(\beta_4, \gamma, \mu) = (-1, 1, 1)$; moreover, $\beta_2 = 0.4$ in (a1)–(c2).

curves with two branches that meet at fold points, where two R_1 -symmetric homoclinic solutions coalesce. For each curve, the upper branch corresponds to the homoclinic solutions associated with the EtoP cycle generated by the connection in Fig. 2(a1) and its R_1 counterpart, while the lower branch corresponds to the homoclinic solutions associated with the EtoP cycle generated by the connection in Fig. 2(a2) and its R_1 counterpart. In Fig. 2(d), we show the bifurcation curves of the homoclinic solutions with two to eight humps; the two curves that are highlighted in darker color correspond to the homoclinic solutions with three and four humps shown in Figs. 2(b1)–2(c2). Notice that all the bifurcation curves associated with the R_1 -symmetric homoclinic solutions of Γ_* fold close to $\beta_2 \approx 0.5753$. Furthermore, as the number of humps of the homoclinic solutions increases, the β_2 values where they fold approach $\beta_2 \approx 0.5753$ from below; that is, they accumulate on the β_2 values where the EtoP connection folds. Also shown in Fig. 2(d) is the curve of the primary homoclinic solution from Fig. 1(c), which exists in the entire β_2 range up to $\beta_2 \approx 0.8164$ where the eigenvalues of $\mathbf{0}$ become purely imaginary at HH.

2. R_1 -symmetry-broken homoclinic solutions

Since there exist two distinct EtoP connections to Γ_* , one can also consider the heteroclinic cycle that is formed by the EtoP connection in Fig. 2(a1) and the R_1 counterpart of the EtoP connection in Fig. 2(a2), or vice versa. The homoclinic solutions associated with these cycles are nonsymmetric and are illustrated in Fig. 3 along with their bifurcation diagram. The homoclinic solution in Fig. 3(a1) can be thought of as a concatenation of the first part of the EtoP connection in Fig. 2(a1) up to its second maximum with the R_1 counterpart of the EtoP connection in Fig. 2(a2) up to its second maximum. If the concatenation is performed the other way around, the homoclinic solution in Fig. 3(a2) is obtained; it is the R_1 counterpart of the homoclinic solution in Fig. 3(a1). By considering one further half-turn around Γ_* , the homoclinic solutions in Figs. 3(b1) and 3(b2) are derived. In this way, nonsymmetric homoclinic solutions for any number of humps can be obtained.

Note that all these nonsymmetric homoclinic solutions also come in pairs, but they are each others R_1 counterparts. Hence, in the bifurcation diagram in Fig. 3(c) the two branches lie on

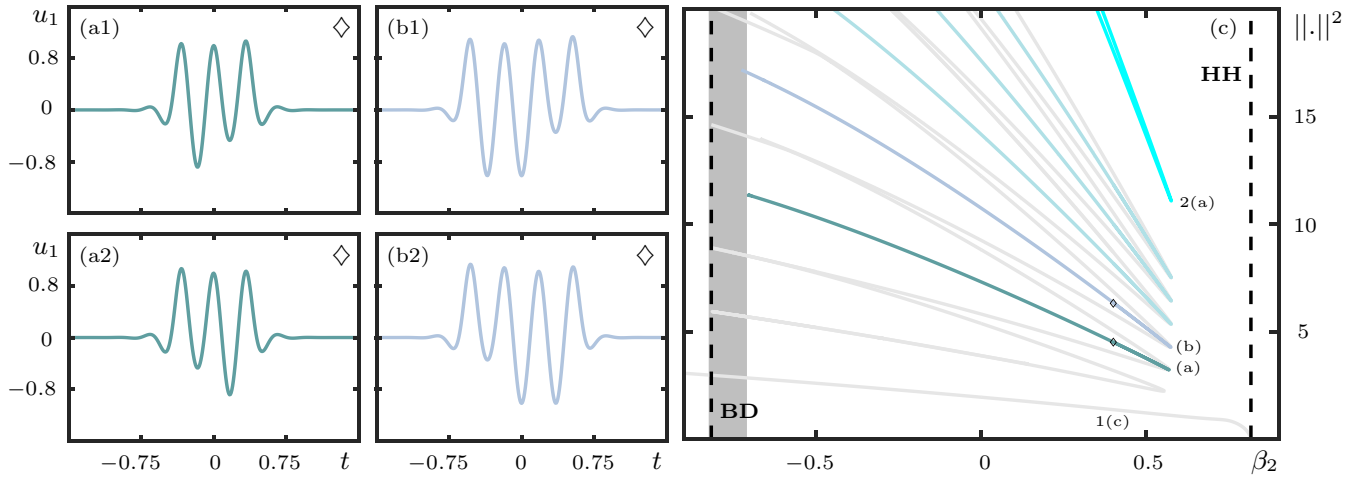


FIG. 3. Family of R_1 -symmetry-broken homoclinic solutions associated with Γ_* . (a), (b) Show temporal traces of nonsymmetric homoclinic solutions associated with the connections shown in Fig. 2(a). (c) Shows the bifurcation diagram in β_2 of the EtoP connections (cyan, top right curve) and R_1 -symmetry-broken homoclinic solutions where solutions are represented by the square of the L_2 norm of their u_1 component. The black diamonds on the bifurcation curves correspond to the solutions shown in (a1)–(b2). (c) Follows the same color and symbol convention as Fig. 2(d) but with respect to the R_1 -symmetry-broken homoclinic solutions; all the homoclinic bifurcation curves from Fig. 2(d) are superimposed in light gray in (c). The bifurcation curves in (c) are for $(\beta_4, \gamma, \mu) = (-1, 1, 1)$; moreover, $\beta_2 = 0.4$ in (a1)–(b2).

top of each other and are indistinguishable. The two branches meet at a fold point at $\beta_2 \approx 0.5753$, and they become R_1 symmetric at this point. As before, we show the bifurcation curves of the EtoP connection and nonsymmetric homoclinic solutions from three to seven humps in Fig. 3(c). In particular, we highlight the bifurcation curves of the three- and four-hump nonsymmetric homoclinic solutions in a darker color; moreover, all curves of the R_1 -symmetric homoclinic bifurcations from Fig. 2(d) are shown in light gray. Note that nonsymmetric and R_1 -symmetric homoclinic solutions with the same number of humps fold at the same β_2 value. That is, in order to transition between corresponding R_1 counterparts of each nonsymmetric homoclinic solution, they must reach a fold point where they become symmetric. Thus, each fold point is a symmetry breaking of the R_1 symmetry. Therefore, we refer to this family of nonsymmetric homoclinic solutions as R_1 -symmetry-broken homoclinic solutions of Γ_* .

3. R_2 -symmetric and R_2 -symmetry-broken homoclinic solutions

There also exist cycles formed by the EtoP connections shown in Fig. 2(a) and their R_2 counterparts. In general, we find a similar phenomenon where the corresponding cycle organizes R_2 -symmetric homoclinic solutions which come in pairs. In particular, these homoclinic solutions intersect the reversibility section Σ_2 transversally at $t = 0$. They symmetry break at fold points and there are also associated pairs of nonsymmetric homoclinic solutions, which are R_2 -symmetry-broken solutions.

Figure 4 shows some representative examples of R_2 -symmetric and R_2 -symmetry-broken homoclinic solutions together with their bifurcation diagram. As for the R_1 -symmetric homoclinic solutions, there exists a basic R_2 -symmetric homoclinic solution with one hump, which is shown in Fig. 4(a1). To illustrate the effect of the R_1 reversibility on these R_2 -symmetric homoclinic solutions, the

R_1 counterpart of this solution is shown in Fig. 4(a2). The homoclinic solutions in Figs. 4(b1), 4(b2) and 4(c1), 4(c2) have one and two further half-turns around Γ_* , respectively. Two nonsymmetric homoclinic solutions are shown in Figs. 4(b3) and 4(c3); they are associated with the EtoP cycle formed by the EtoP connections in Fig. 2(a1) and the R_2 counterpart of the EtoP connection in Fig. 2(a2).

Figure 4(d) shows the bifurcation diagram of the R_2 -symmetric and nonsymmetric homoclinic solutions up to seven humps, and we highlight the ones with two and three humps in darker color. Here, all the previously shown homoclinic bifurcation curves are shown in light gray. The basic R_2 -symmetric homoclinic solution and its R_1 counterpart shown in Fig. 4(a) exist throughout the β_2 interval where $\mathbf{0}$ has complex-conjugate eigenvalues. On the other hand, all the other R_2 -symmetric homoclinic solutions lie again on curves with two branches that meet at fold points. The new nonsymmetric homoclinic solutions also come in pairs. Since they have the same L_2 norm, the respective two branches of the bifurcation curves lie on top of each other. All nonsymmetric homoclinic solutions become R_2 symmetric at the coinciding fold points; here the R_2 symmetry is broken, which is why we refer to them as R_2 -symmetry-broken homoclinic solutions. As the number of humps per homoclinic solution increases, the parameter values where they fold accumulate on $\beta_2 \approx 0.5753$; notice, however, that this accumulation is now from larger values of β_2 .

4. Connection with homoclinic snaking

It is clear from Fig. 4(d) that only the bifurcation curves of the primary R_1 - and R_2 -symmetric homoclinic solutions reach the HH bifurcation; the bifurcation curves of multihump R_1 - and R_2 -symmetric homoclinic solutions, on the other hand, have folds before reaching HH. When viewed for decreasing β_2 , the two branches of primary homoclinic solutions

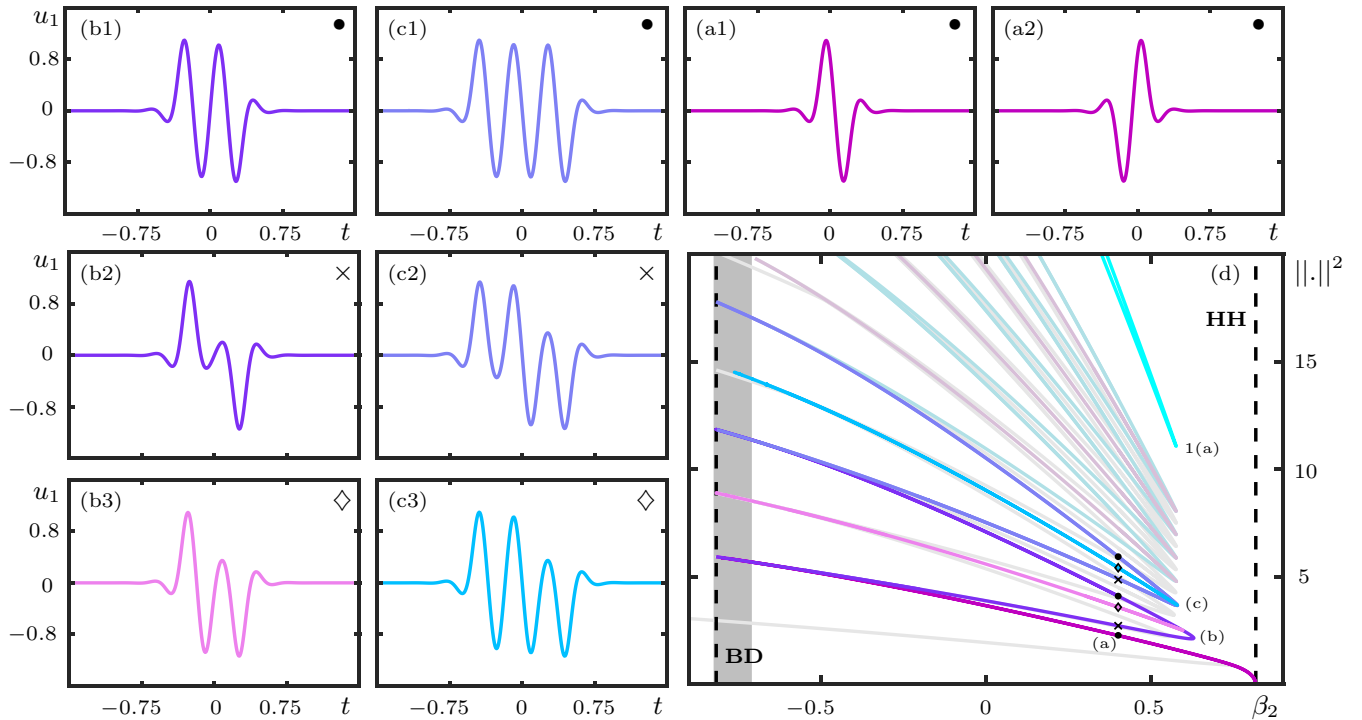


FIG. 4. Family of R_2 -symmetric and R_2 -symmetry-broken homoclinic solutions associated with Γ_* . (a) Show the temporal traces of the basic R_2 -symmetric homoclinic solution and its corresponding R_1 -symmetric counterparts. (b1), (c1) and (c2), (c3) Show the temporal traces of the R_2 -symmetric homoclinic solutions associated with the EtoP connections shown in Figs. 2(a1) and 2(a2), respectively. (b2), (c2) Show nonsymmetric homoclinic solutions with one and two humps, respectively. (d) Shows the bifurcation diagram in β_2 of the EtoP connections (cyan, top right curve) and corresponding homoclinic solutions, where solutions are represented by the square of the L_2 norm of their u_1 component. (d) Follows the color and symbol convention as Fig. 2(d) but with respect to the R_2 -symmetric and R_2 -symmetry-broken homoclinic solutions; all the homoclinic bifurcation curves from Figs. 2(d) and 3(c) are superimposed in light gray in (d). The bifurcation curves in (d) are for $(\beta_4, \gamma, \mu) = (-1, 1, 1)$; moreover, $\beta_2 = 0.4$ in (a1)–(c3).

emerge from the HH bifurcation. It has been observed in other four-dimensional reversible systems [42], including the Swift-Hohenberg equation [18] and the Lugiato-Lefever equation (LLE) [17], that these primary homoclinic curves born at the HH bifurcation can undergo a phenomenon known as *homoclinic snaking*: these two branches of homoclinic solutions fold back and forth repeatedly when continued in a chosen parameter. Moreover, there exist branches of symmetry-broken homoclinic solutions that connect the two branches of symmetric homoclinic solutions at respective fold points; these symmetry-broken branches are also referred to as “rungs” because they form a ladderlike structure with the two primary branches.

The bifurcation structure we find here for system (5) in Figs. 2–4 is quite similar in spirit, but the bifurcation curves of all homoclinic solutions end for decreasing β_2 at the BD bifurcation rather than featuring fold bifurcation on the left as well. This type of bifurcation structure due to the existence of the BD bifurcation, which we refer to as *BD-truncated homoclinic snaking*, was observed, for example, in [17] in a certain parameter regime of the LLE. In contrast to the LLE, changing any of the parameters of system (5) does not qualitatively change the bifurcation diagram in Fig. 4(d), as can be seen from the nondimensionalization. Thus, one cannot find full homoclinic snaking in system (5).

The absence of full homoclinic snaking means, in particular, that the branches of symmetric homoclinic solutions with increasing numbers of humps of system (5) do not form two single connected branches. Hence, they cannot be obtained simply by continuation of the two primary homoclinic solutions through successive fold points but must be found one by one. As was explained in Sec. III, this can be achieved efficiently with Lin’s method. This approach has the additional advantage that it allows us to also find and continue the underlying EtoP connections, which organize the respective branches of homoclinic solutions with different symmetry properties. Finding branches of EtoP connections is a new aspect of our work, which shows that the β_2 values of the fold points of homoclinic solution curves accumulate, as the number of humps increases, on the β_2 value of the fold of the underlying EtoP connection. As we will show next, there are more such EtoP connections, including those to periodic solutions with less symmetry.

B. Homoclinic solutions associated with R_1 -symmetric periodic solution

It is possible to have a (pair of) periodic solutions with only R_1 symmetry in the zero-energy level. We find that there are EtoP connections between $\mathbf{0}$ and these periodic solutions for

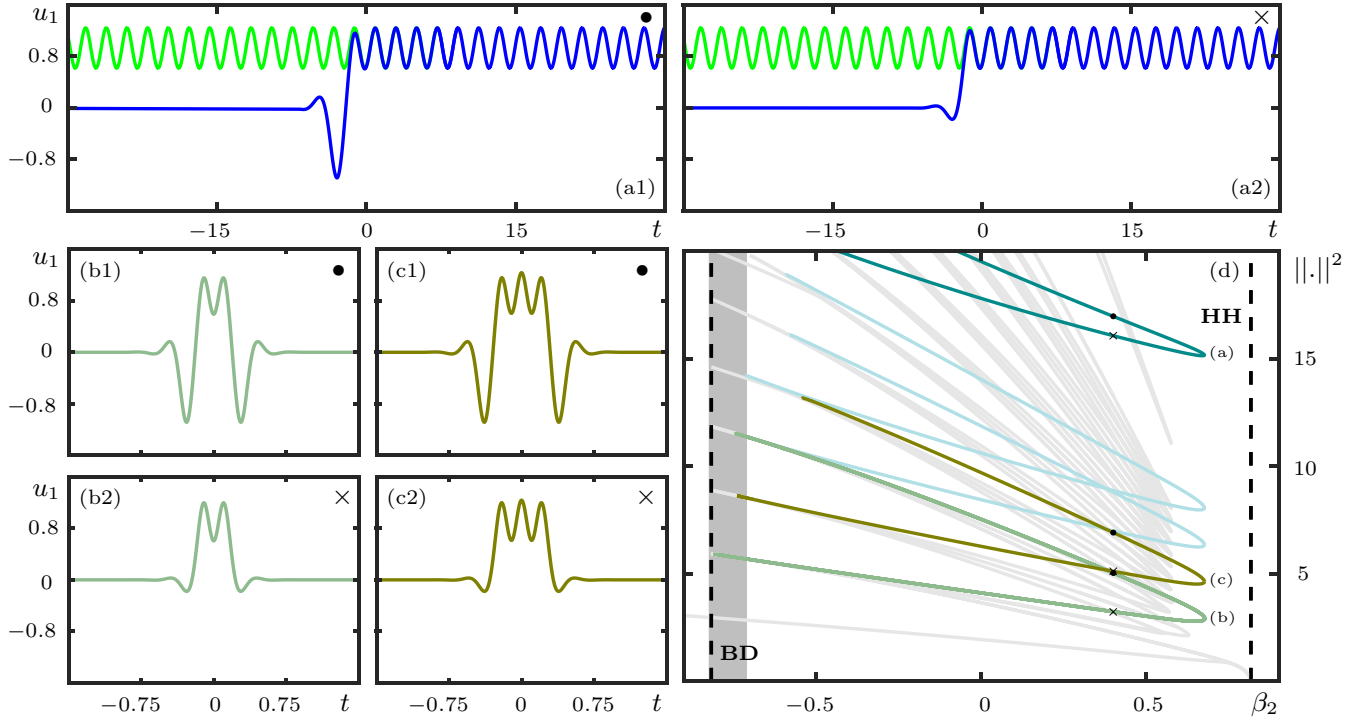


FIG. 5. Family of R_1 -symmetric homoclinic solutions associated with R_1 -symmetric periodic solution. (a1), (a2) Show two connections (blue curves, starting at 0) between $\mathbf{0}$ and a periodic solution Γ_1^+ (green oscillating curve) that is only invariant under R_1 . (b1),(c1) and (b2),(c2) Show temporal traces of R_1 -symmetric homoclinic solutions, associated with the connections shown in (a1) and (a2), respectively. (d) Shows the bifurcation diagram in β_2 of the EtoP connections (dark cyan, top right curve) and R_1 -symmetric homoclinic solutions, where solutions are represented by the square of the L_2 -norm of their u_1 component. All the bifurcation curves from Fig 2(d), Fig. 3(c) and Fig. 4(d) are superimposed in light grey. (d) Follows the color and symbol convention as Fig. 2(d) but with respect to the R_1 -symmetric homoclinic solutions associated with R_1 -symmetric periodic solution. The bifurcation curves in (d) are for $(\beta_4, \gamma, \mu) = (-1, 1, 1)$; moreover, $\beta_2 = 0.4$ in panels (a1)-(b2).

certain parameter values. As before, there are associated R_1 -symmetric homoclinic solutions that come in pairs and meet at fold points, where they also symmetry break. However, we do not find R_2 -symmetric and R_2 -symmetry-broken homoclinic solutions associated with these EtoP connections. Families of R_1 -symmetric and R_1 -symmetry-broken homoclinic solutions associated with an R_1 -symmetric periodic solution are shown, respectively, in Figs. 5 and 6.

Figure 5 shows the R_1 -symmetric homoclinic solutions in the same layout as Fig. 2. Figures 5(a1) and 5(a2) show two EtoP connections, but now to an R_1 -symmetric periodic solution Γ_1^+ . Note that throughout this paper, the R_2 counterpart of Γ_1^+ is denoted by Γ_1^- , and that any results pertaining to homoclinic solutions and EtoP connections of Γ_1^+ also apply to Γ_1^- . The EtoP connections in Fig. 5(a) are not related by symmetry: the one in Fig. 5(a1) has a larger negative excursion in u_1 before converging to Γ_1^+ compared to that in Fig. 5(a2). Associated with the EtoP cycles generated by the EtoP connections in Fig. 5(a) and their corresponding R_1 counterparts, one can find R_1 -symmetric homoclinic solutions that make any number of turns around Γ_1^+ . Figures 5(b1) and 5(c1) show homoclinic solutions with one full turn around Γ_1^+ , and Figs. 5(b2) and 5(c2) those with one further half-turn around Γ_1^+ . Figure 5(d) shows the corresponding bifurcation diagram, where the two EtoP connections occur on a branch that folds at $\beta_2 \approx 0.6756$; they are again represented

by a finite norm (by truncating them after eight oscillations around the periodic solution). Also shown are curves of the R_1 -symmetric homoclinic solutions from two to five humps, where the ones in Figs. 5(b) and 5(c) are highlighted in darker color. The curves of R_1 -symmetric homoclinic solutions all have folds and, as the number of humps increases, the β_2 values where they fold accumulate onto that of the fold of EtoP connections of Γ_1^+ .

Figure 6 illustrates the R_1 -symmetry-broken homoclinic solutions, which are associated with the EtoP cycle generated by the EtoP connection in Fig. 5(a1) and the R_1 counterpart of the EtoP connection in Fig. 5(a2), or vice versa. In Fig. 6(a) these homoclinic solutions have one turn around Γ_1^+ , while in Fig. 6(b) they make one further half-turn. Moreover, the homoclinic solutions in Figs. 6(a2) and 6(b2) are the R_1 counterparts of those in Figs. 6(a1) and 6(b1). As the bifurcation diagram in Fig. 6(c) shows, the R_1 -symmetry-broken homoclinic connections can be found along curves that have folds at the fold points on the curves of R_1 -symmetric homoclinic connections (light gray). Here, we highlight the curves of the R_1 -symmetry-broken homoclinic solutions with two and three humps in darker color; the respective two branches are again indistinguishable in Fig. 6(c) because they have the same L_2 norm.

All these curves in Figs. 5(d) and 6(c) of homoclinic connections associated with Γ_1^+ extend on the left to the BD

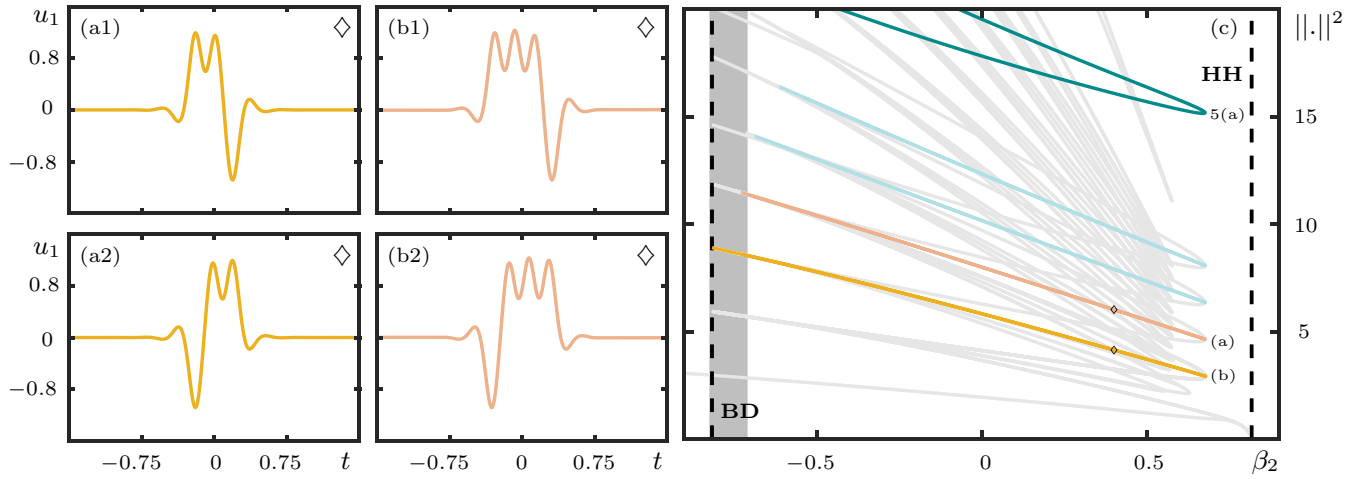


FIG. 6. Family of R_1 -symmetry-broken homoclinic solutions associated with Γ_1^+ . (a), (b) Show temporal traces of nonsymmetric homoclinic solutions associated with the connections shown in Fig. 5(a). (c) Shows the bifurcation diagram in β_2 of the EtoP connections (dark cyan, top right curve) and R_1 -symmetry-broken homoclinic solutions where solutions are represented by the square of the L_2 norm of their u_1 component. (c) Follows the color and symbol convention as Fig. 2(d) but with respect to the R_1 -symmetry-broken homoclinic solutions associated with R_1 -symmetric periodic solution; furthermore, all the previously shown homoclinic bifurcation curves are superimposed in light gray in (c). The bifurcation curves in (d) are for $(\beta_4, \gamma, \mu) = (-1, 1, 1)$; moreover, $\beta_2 = 0.4$ in (a1)–(b2).

bifurcation and, therefore, constitute a further instance of BD-truncated homoclinic snaking. In contrast to the bifurcation curves of the homoclinic solutions associated with Γ_* , there do not exist two primary homoclinic bifurcation curves that arise from the HH point. Notice also that the homoclinic solutions associated with Γ_1^+ exist over a larger β_2 interval; this is due to the fact that the fold of the bifurcation curve of EtoP connection to Γ_1^+ has a considerably larger β_2 value than the fold of the bifurcation curve of EtoP connection to the periodic solution Γ_* .

V. EXISTENCE OF SOLITONS IN TWO-PARAMETER PLANES

As we have seen in the previous sections for fixed $(\beta_4, \mu, \gamma) = (-1, 1, 1)$, infinitely many homoclinic solutions and associated EtoP connections are created at the BD bifurcation, while only the two primary homoclinic solutions reach the HH bifurcation. All other homoclinic solutions and the EtoP connections disappear at fold bifurcations. We know from Sec. II that the BD and HH bifurcations occur along the left and right halves of a parabola in the (β_2, μ) plane of Fig. 1(a) and also in the (β_2, β_4) plane. The folds of homoclinic solutions and EtoP connections are well-defined codimension-one bifurcations that we can continue numerically as curves in these parameter planes. However, this is not necessary because, as we show now, all fold bifurcations also occur along half-parabolas in either of these planes; in particular, they do not depend on the parameter γ and they always occur in the same order as a function of β_2 .

To see this, we consider the ansatz $U(x, \tau) = \hat{u}(\tau)e^{iqx}$ with the nondimensionalization of the GNLSE (1) for $\beta_2 > 0$ and $\beta_4 < 0$ to obtain the ODE

$$\frac{d^4 \hat{u}}{d\tau^4} + \frac{d^2 \hat{u}}{d\tau^2} + q\hat{u} - \hat{u}^3 = 0. \quad (14)$$

The transformation

$$\bar{u} = \sqrt{\frac{-\beta_4 \gamma}{6\beta_2^2}} u, \quad \tau_0 = \sqrt{\frac{-12\beta_2}{\beta_4}} t$$

allows us to rewrite Eq. (4) as

$$\frac{d^4 \bar{u}}{d\tau_0^4} + \frac{d^2 \bar{u}}{d\tau_0^2} - \frac{\beta_4 \mu}{6\beta_2^2} \bar{u} - \bar{u}^3 = 0. \quad (15)$$

Direct comparison between the coefficients of Eq. (14) and those of Eq. (15) gives

$$6q\beta_2^2 + \beta_4 \mu = 0. \quad (16)$$

This relationship extends the results of our bifurcation analysis from the previous sections for fixed β_4 and μ to the whole (β_2, β_4, μ) space. Notice that the value of γ does not influence the location of the fold bifurcations, as this parameter only affects the amplitude of the homoclinic solution. Indeed, Eq. (16) shows specifically that all curves of codimension-one bifurcations with $\beta_2 > 0$ and $\beta_4 < 0$ are half-parabolas in both the (β_2, β_4) plane for fixed μ and in the (β_2, μ) plane for fixed β_4 ; the respective parabola is determined from the computed β_2 values for fixed β_4 and μ by determining the respective value of q in Eq. (16).

Figure 7 illustrates this result by showing the half-parabolas of all folds of EtoP connections and multihump homoclinic solutions we detected. Figure 7(a1) shows the (β_2, β_4) plane for $\mu = 1$ and Fig. 7(b) shows the (β_2, μ) plane for $\beta_4 = -1$, respectively; here $\gamma = 1$. Also shown are the bifurcation curves BD and HH, as well as the half-parabola along which one finds the Karlson and Höök solution [5] (which lies to the left of BD as it concerns solitons with nonoscillating decaying tails). Notice from Fig. 7(a1) that, for fixed quadratic dispersion $\beta_2 > 0$, different families of homoclinic solutions arise as the quartic dispersion β_4 is decreased, namely, at definite negative threshold β_4 values

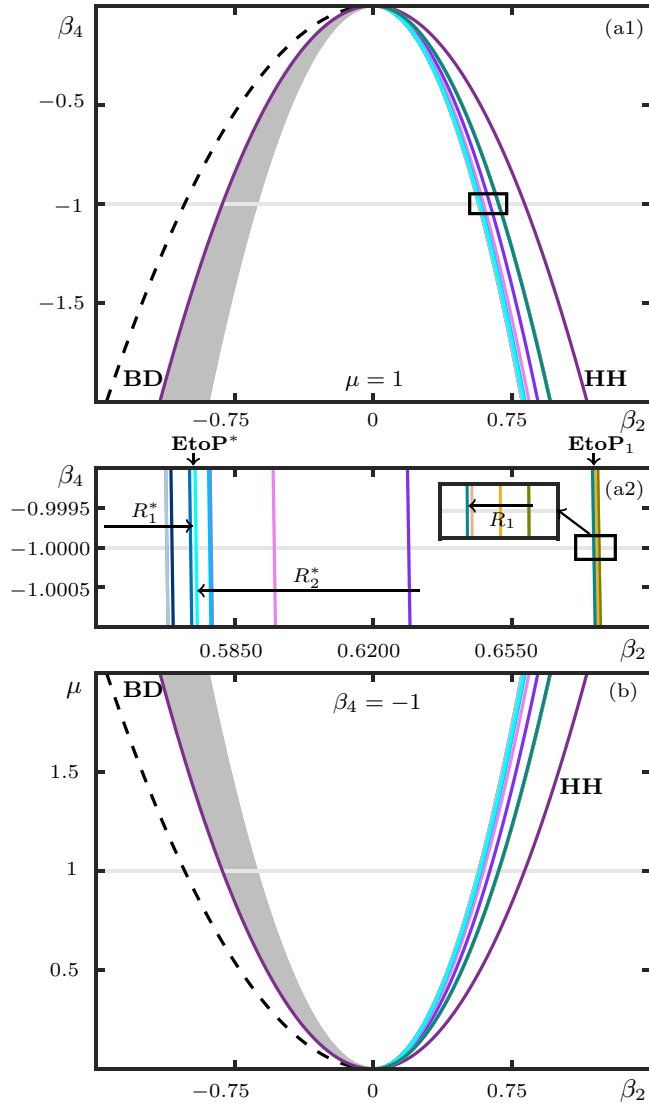


FIG. 7. Bifurcation diagrams in the (β_2, β_4) plane for $(\mu, \gamma) = (1, 1)$ in (a) and in the (β_2, μ) plane for $(\beta_4, \gamma) = (1, 1)$ in (b). Shown are curves of the bifurcations BD and HH (outer parabola) together with curves of folds of the identified EtoP connections and homoclinic solutions (colors as in previous figures); the black dashed curve represents the family of Karlsson-Höök solutions. (a2) Enlargement of the rectangular region in (a1) illustrating the ordering and accumulation of different fold curves, namely, those of R_1 - and R_2 -symmetric homoclinic solutions onto the EtoP connection **EtoP*** to Γ_* , and those of the R_1 -symmetric homoclinic solutions onto the EtoP connection **EtoP₁** to Γ_1^+ (enlarged further in the inset).

given by the half-parabolas of fold bifurcations. Figure 7(a2) is an enlargement of the rectangular region near $\beta_4 = -1$ in Fig. 7(a1) that illustrates how the curves of the homoclinic solutions associate with Γ_* and Γ_1^+ accumulate on the two basic EtoP connections from Sec. IV A, labeled here **EtoP***, and from Sec. IV B, labeled here **EtoP₁**.

As Fig. 7 shows, the ordering of these bifurcation curves is exactly the same in the (β_2, μ) plane in Fig. 7(b); compare with Fig. 1(a). Importantly, μ is not a system parameter of the GNLSE (1) but arises from the ansatz (3). Therefore, moving

along any vertical line in Fig. 7(b) does not change any of the dispersion terms of the GNLSE. Moreover, for given quartic dispersion β_4 , there is a critical μ value for solitons to exist. Therefore, by increasing the wave number μ , for given fixed values of β_2 , β_4 , and γ , one can generate many more homoclinic solutions and, therefore, different solitons of (1).

VI. INFINITELY MANY PERIODIC SOLUTIONS WITH ZERO ENERGY

As the previous sections show, periodic solutions of system (5) in the zero-energy surface with R^* or R_1 symmetry give rise, via the existence of EtoP connections, to BD-truncated homoclinic snaking. We now show that there are in fact infinitely many R^* -symmetric and R_1 -symmetric periodic solutions with zero energy and, hence, many more families of homoclinic solutions of the equilibrium $\mathbf{0}$ with different symmetry properties. All of these homoclinic solutions indeed correspond to solitons of the GNLSE.

In what follows and specifically in Fig. 8, we show representative solutions of system (5) in phase space in different representations. Hence, periodic and homoclinic solutions now correspond to periodic and homoclinic orbits in phase space; see already Figs. 8(a) and 8(b). These panels show in the (u_1, u_2) plane the basic R_1 -symmetric homoclinic orbit and the periodic orbits we considered in Sec. IV, for $(\beta_2, \beta_4, \mu, \gamma) = (0.4, -1, 1, 1)$. Notice that the basic R_1 -symmetric homoclinic orbits come as a pair, and each of them spirals near the point $\mathbf{0}$ due to its complex-conjugate eigenvalues. On the other hand, the periodic orbits in Fig. 8(b) are closed loops; the R^* -symmetric periodic orbit Γ^* is a single loop, while the R_1 -symmetry periodic orbits $\Gamma_1^{+/-}$ come in pairs, which are each others R_2 counterparts.

Given that system (5) is reversible, for fixed values of the system parameters, periodic orbits come in one-parameter families; moreover, each homoclinic orbit gives rise to a one-parameter family of periodic orbits [22,23]. Each periodic orbit can only be in a specific energy level H , which is why we consider them here as surfaces in (u_1, u_2, H) space. This representation has the added advantage that it allows us to easily identify periodic orbits that are in the zero-energy level. Specifically, we consider three surfaces of periodic orbits, which we find by continuation in the energy H from the primary homoclinic orbit and its R_2 counterpart in Fig. 8(a): individually, these two homoclinic orbits each give rise to R_1 -symmetric periodic orbits, which are each others R_2 counterparts, while their union gives rise to R^* -symmetric periodic orbits.

Figures 8(c) and 8(d) show these periodic orbits for $(\beta_2, \beta_4, \mu, \gamma) = (0.4, -1, 1, 1)$. Namely, Fig. 8(c) shows three surfaces of periodic orbits in (u_1, u_2, H) space in a cutaway view that only shows their parts for positive u_2 ; note that the missing parts can be obtained by application of R_1 , which is reflection in the (u_1, H) plane. Here, in Fig. 8(c), the surfaces that contain the periodic orbits Γ^* and $\Gamma_1^{+/-}$ are denoted \mathcal{S}_* and $\mathcal{S}_1^{+/-}$, respectively. Also shown are six selected periodic orbits in the zero-energy level. Figure 8(d) shows the respective intersection curves in the (u_1, H) plane, where the selected periodic orbits are identified as points with

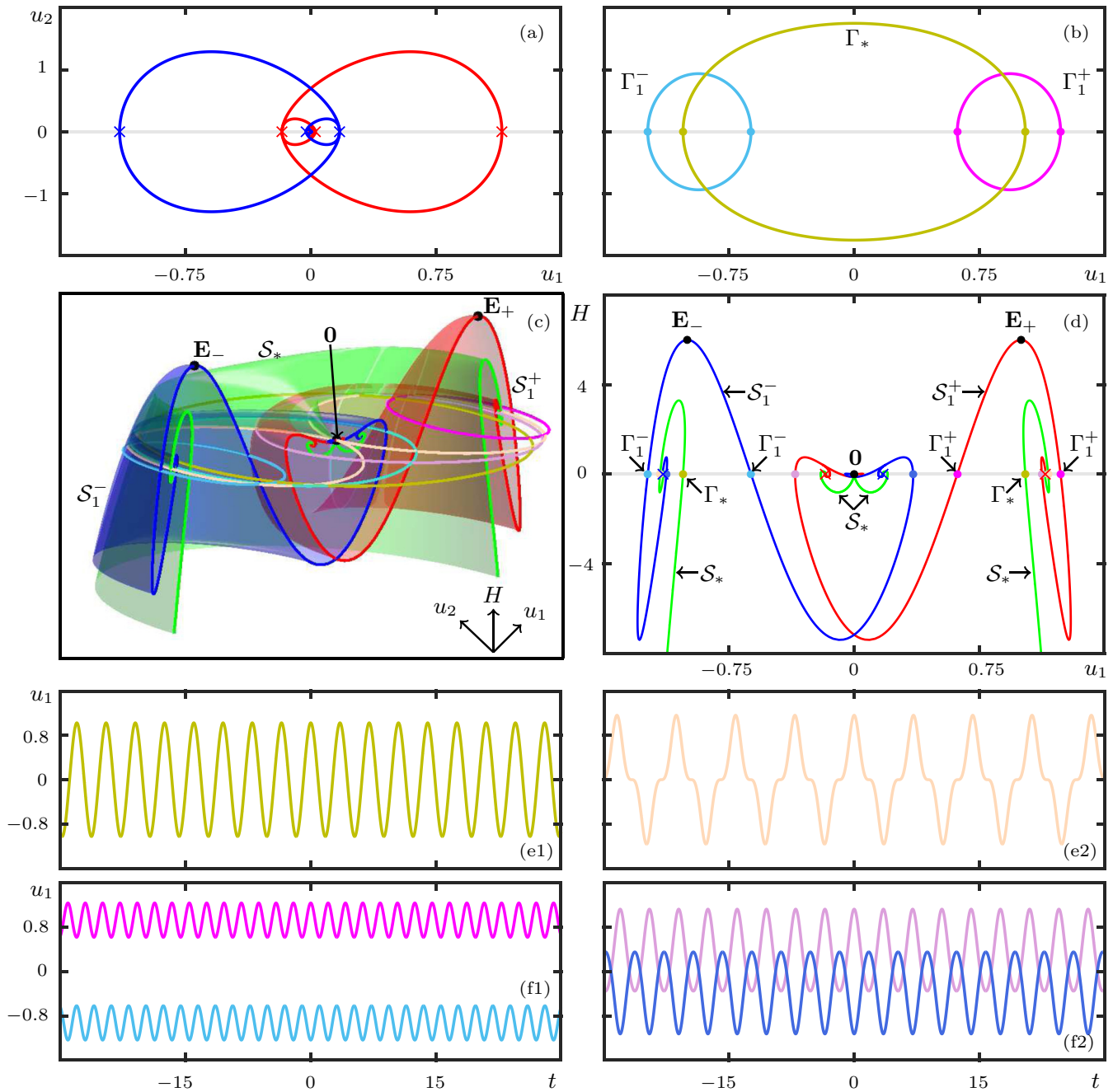


FIG. 8. Existence of periodic solutions of system (5) for $(\beta_2, \beta_4, \gamma, \mu) = (0.4, -1, 1, 1)$. (a), (b) Show, in the (u_1, u_2) plane, the basic R_1 -symmetric homoclinic orbit with its R_2 counterpart and the three periodic orbits Γ_* and $\Gamma_1^{+/-}$ with $H(\mathbf{u}) = 0$. In both panels the light-gray line represents $u_2 = 0$, with crosses and circles indicating the intersections of the homoclinic and periodic orbits, respectively. (c) Shows, in (u_1, u_2, H) space, half of the two-dimensional surfaces formed by three families of periodic solutions, referred to as S_1^+ (red surface), S_1^- (blue surface), and S_* (green surface), with R_1 and R^* symmetry, respectively. The black dots represent the three equilibria of system (5); also shown are six periodic orbits in the zero-energy level. Their temporal profiles are also presented; namely, (e1) and (e2) show Γ_* and a secondary R^* -symmetric periodic orbit, respectively; (f1) shows Γ_1^+ (top) and Γ_1^- (bottom), and (f2) a secondary R_1 -symmetric periodic orbit (top) and its R_2 counterpart (bottom). (d) Shows the intersection curves of the each surface with $u_2 = 0$; the light gray line represents $H(\mathbf{u}) = 0$. The intersection points of each periodic solution in (e1)–(f2) are indicated by circles, and the intersection points of the basic homoclinic solution and its R_1 counterpart by crosses.

$H = 0$. Figure 8(e1) shows Γ_* from Sec. IV A and Fig. 8(f1) shows $\Gamma_1^{+/-}$ from Sec. IV B. Similarly, Figs. 8(e2) and 8(f2) show additional R^* -symmetric and R_1 -symmetric periodic solutions, respectively.

Notice in Fig. 8(c), and even more clearly in Fig. 8(d), that the surface S_1^+ has a global maximum in H at \mathbf{E}_+ , which lies in the $H(\mathbf{E}_+)$ -energy level. Moreover, it has a global minimum in H when it reaches a periodic orbit with $H(\mathbf{u}) \approx -7.4$.

Thus, the Hamiltonian of this family of periodic orbits is bounded between these two values. The same statement is of course true for the surface \mathcal{S}_1^- , but its global maximum is the equilibrium \mathbf{E}_- , which is the R_2 counterpart of \mathbf{E}_+ . The pair $\Gamma_1^{+/-}$ in Fig. 8(f1) corresponds to the first intersection with $H(\mathbf{u}) = 0$ of this pair of surfaces when continued from \mathbf{E}_+ and \mathbf{E}_- .

The surface \mathcal{S}_* has a global maximum when it reaches a periodic orbit with $H(\mathbf{u}) \approx 3.3$, but it does not have a global minimum in H ; indeed, our numerical continuation results strongly suggest that this surface extends to any negative value of H . Note from Figs. 8(c) and 8(d) that, while its intersection with the (u_1, H) plane consists of three components, the surface \mathcal{S}_* is nevertheless connected. The periodic solution Γ_* in Fig. 8(e1) is at the first intersection of this surface with $H(\mathbf{u}) = 0$, when continued for increasing H from large negative values.

The surfaces \mathcal{S}^+ and \mathcal{S}^- accumulate on the basic R_1 -symmetric homoclinic orbit and its R_2 counterpart, respectively. On the other hand, the surface \mathcal{S}_* accumulates on the union of the basic R_1 -symmetric homoclinic orbit and its R_2 counterpart. This is not so easy to see in the three-dimensional projection in Fig. 8(c), but it can be observed more clearly in the (u_1, H) plane in Fig. 8(d). Notice that the respective intersection curves spiral into the intersection points of the two homoclinic orbits (marked by crosses), which means that these curves cross $H(\mathbf{u}) = 0$ infinitely often in the process. Hence, there are infinitely many additional periodic solutions with R^* and R_1 symmetry in the zero-energy level. Figures 8(e2) and 8(f2) show the next such periodic solutions when continued on from the primary ones shown in Figs. 8(e1) and 8(f1), respectively. Each of these periodic orbits with $H(\mathbf{u}) = 0$ has a connection with $\mathbf{0}$ in certain parameter ranges. These infinitely many EtoP connections each give rise to BD-truncated homoclinic snaking scenarios with infinitely many homoclinic connections, with R^* and R_1 symmetry of the kind we presented in Secs. IV A and IV B.

The picture that emerges from the discussion of only the surfaces \mathcal{S}_* and $\mathcal{S}_1^{+/-}$ discussed here is indeed rather intriguing: each new homoclinic orbit gives rise to families of R^* - and R_1 -symmetric periodic orbits, which, due to their spiraling create yet more periodic orbits in the zero-energy surface. Hence, there are infinite cascades of EtoP connections with infinitely many homoclinic orbits creating infinitely many new surfaces generating infinitely many periodic orbits each and so on. Moreover, there also exist more complicated connections associated with different periodic orbits, such as connections from a periodic orbit to itself (homoclinic orbits to a periodic orbit) and heteroclinic connections from one periodic orbit to another (PtoP connections) [43]. All these connections between periodic orbits also form more complex heteroclinic cycles. Therefore, there exist infinitely many additional homoclinic and periodic orbits that involve PtoP connections. How the different surfaces of periodic orbits are organized in phase space, and how this geometric structure changes as parameters are varied, is an interesting and challenging question. However, this is beyond the scope of this paper and will be discussed elsewhere.

VII. STABILITY PROPERTIES OF THE DIFFERENT TYPES OF SOLITONS

The R_1 -symmetric primary soliton from Fig. 1(c) was considered by Tam *et al.* [2–4] and found to be linearly stable in any parameter range. As we have just shown, there exist infinitely many other solitons with different symmetry properties over a broad parameter range of β_2 , including for the case of a quartic fiber with $\beta_2 = 0$. It seems natural to suspect that all these other (multihump) solitons are linearly unstable. Determining the stability of soliton solution of a PDE is a challenging task [44], and we restrict ourselves here to providing some first insights into the stability of the different types of solitons by means of simulations of the GNLSE with a split-step Fourier method (SSFM) [19]. More specifically, we construct the respective soliton $u(t)$ from the particular homoclinic solution in Sec. IV. We then perturb $u(t)$ in the same specific way as considered in [3], namely, by increasing its size, here by 1%; that is, by considering the scaled profile $1.01u(t)$ as the input. We then evolve this perturbed profile with the SSFM with suitable accuracy settings to see how long it remains close to the initial constructed soliton, that is, propagates seemingly stably along the fiber before breaking up. In this way, we obtain an indication of whether and which multihump solitons might be observable in a physical experiment.

The simulations we performed are in no way exhaustive or representative of the different kinds of perturbations one may encounter in an experiment. Nevertheless, they do provide some insights into differences in stability of the various types of solitons. Perturbations of the R_1 -symmetric primary soliton from Fig. 1(c) die down during the simulation, meaning that this soliton can be propagated with the SSFM for an arbitrarily long distance along the fiber; this fact was used to determine suitable accuracy setting (determining time and space discretizations) for the SSFM.

Figures 9 and 10 show for fixed $(\beta_4, \mu, \gamma) = (-1, 1, 1)$ and for $\beta_2 = -0.2$, $\beta_2 = 0$, and $\beta_2 = 0.2$ the intensity profiles of different types of 1%-perturbed solitons with their evolutions along the fiber as computed with the SSFM. More specifically, we consider the two-hump R_1 -symmetric soliton in Figs. 9(a)–9(c) and the primary R_2 -symmetric soliton in Figs. 9(d)–9(f). Likewise, Fig. 10 shows the three-hump R_1 -symmetric soliton in panels 10(a)–10(c) and the corresponding R_1 -symmetry-broken soliton in panels 10(d)–10(f). In each case, the bottom panel shows the initial intensity profile (at $z = 0$), with the temporal trace of the corresponding homoclinic solution in the top-right corner; the top panel shows the evolution of the respective initial 1%-perturbed intensity profile.

As Figs. 9 and 10 show, all of these 1%-perturbed solitons break up after some finite distance, which supports the conjecture that they are indeed unstable. However, we find considerable differences between different initial solutions in how far along the fiber they can be propagated before breaking up. The differences manifest themselves for pure quartic solitons with $\beta_2 = 0$, the case that motivated our study, but also depend on the value β_2 of the quadratic dispersion. To quantify the effective distance over which a 1%-perturbed soliton may be observed in practice, we scale the fiber coordinate z

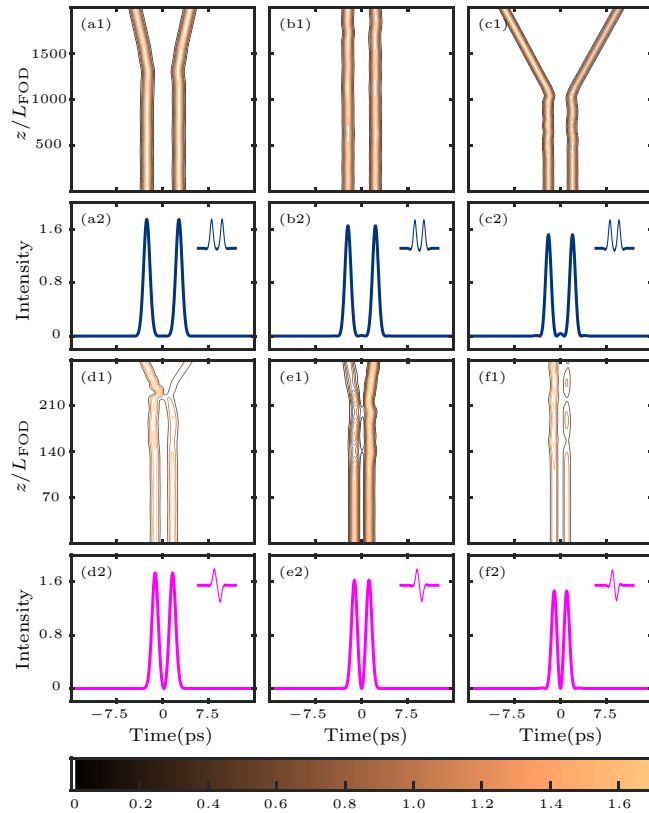


FIG. 9. Evolution of the 1%-perturbed R_1 -symmetric two-hump soliton in (a)–(c) and the R_2 -symmetric primary soliton in (d)–(f), for fixed $(\beta_4, \mu, \gamma) = (-1, 1, 1)$ and $\beta_2 = -0.2$, $\beta_2 = 0$, and $\beta_2 = 0.2$, respectively. For each case, the bottom panel shows the initial intensity profile, with the temporal trace of the corresponding homoclinic solutions in the top right, while the top panel shows the evolution as computed with the SSFM.

by the fourth-order dispersion length of a pulse given by

$$L_{\text{FOD}} = \frac{T_0^4}{|\beta_4|}.$$

Here $T_0 = \text{FWHM}/2\sqrt{\log 2}$ is determined from the full width at half-maximum (FWHM) of the pulse; this is exact for a Gaussian (intensity) pulse, and a good approximation for pulses that are close to Gaussian [19]. For initial 1%-perturbed multihump solitons in Figs. 9 and 10, which all feature quite distinctive pulses, we consider the largest pulse and find that a Gaussian is still a good fit; hence, we determine L_{FOD} from the FWHM of the largest pulse. We found that the values of the computed fourth-order dispersion length L_{FOD} of all initial solitons we considered agree up to two decimal places with that of the R_1 -symmetric primary soliton, which we determined as $L_{\text{FOD}} = 0.29$ for $\beta_2 = -0.2$, $L_{\text{FOD}} = 0.22$ for $\beta_2 = 0$, and $L_{\text{FOD}} = 0.16$ for $\beta_2 = 0.2$. Furthermore, we computed from the FWHM the group velocity dispersion length $L_{\text{GVD}} = T_0^2/|\beta_2|$ (second-order dispersion) for $\beta_2 = -0.2$ and 0.2 . For all the initial 1%-perturbed solitons we consider, L_{GVD} is one order of magnitude larger than L_{FOD} . We conclude that the fourth-order dispersion is clearly dominant and, therefore, we use the above values of L_{FOD} to scale z in Figs. 9 and 10.

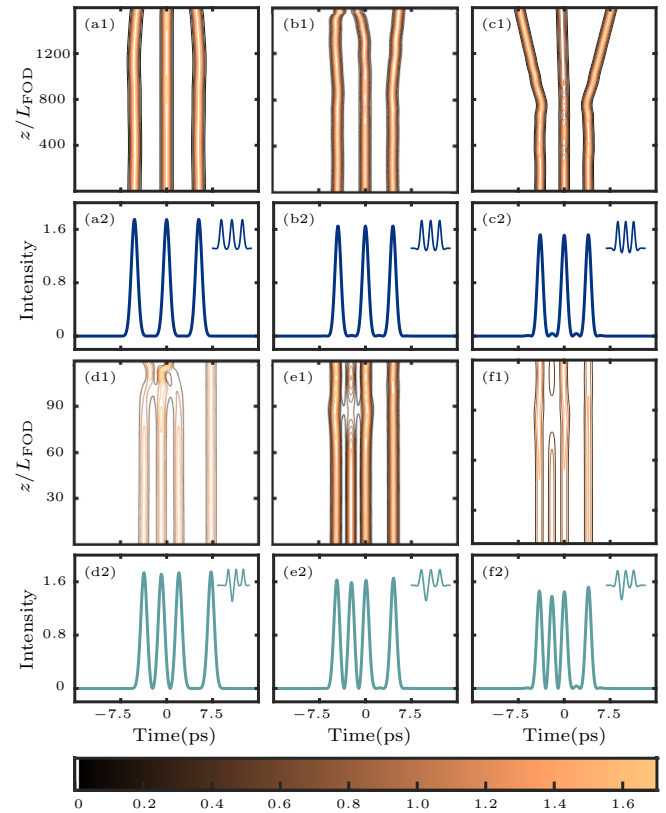


FIG. 10. Evolution of the 1%-perturbed R_1 -symmetric three-hump soliton in (a)–(c) and the corresponding symmetry-broken soliton in (d)–(f), for fixed $(\beta_4, \mu, \gamma) = (-1, 1, 1)$ and $\beta_2 = -0.2$, $\beta_2 = 0$, and $\beta_2 = 0.2$, respectively. For each case, the bottom panel shows the initial intensity profile, with the temporal trace of the corresponding homoclinic solutions in the top right, while the top panel shows the evolution as computed with the SSFM.

The two-hump R_1 -symmetric soliton in Figs. 9(a)–9(c) is only weakly unstable and can be observed over up to $1500 L_{\text{FOD}}$ in a quartic-dispersion fiber with $\beta_2 = 0$ before breaking up; with small second-order dispersion of $\beta_2 = -0.2$ and 0.2 this value drops to 1250 and $1000 L_{\text{FOD}}$, respectively. By contrast, the primary R_2 -symmetric soliton in Figs. 9(d)–9(f) is considerably more unstable and is observable only up to $120 L_{\text{FOD}}$ for the three considered values of β_2 ; beyond this value of L_{FOD} we observe noticeable interactions between the two intensity pulses and pulse breakup shortly thereafter. As Figs. 10(a)–10(c) show, the perturbed three-hump R_1 -symmetric soliton is observable considerably farther along the fiber, up to about $600 L_{\text{FOD}}$ for all β_2 , after which pulse interactions become visible and the soliton breaks up. Note that negative β_2 increases the observation length, while positive β_2 decreases it. The related R_1 -symmetry-broken soliton in Figs. 10(d)–10(f) is clearly much more unstable and can be observed only up to about $60 L_{\text{FOD}}$.

Our preliminary simulation results suggest that R_1 -symmetric solitons with two and with three humps are only weakly unstable. This means that, when launched quite precisely into an actual quartic dispersion fiber, they might be sustained over a sufficiently large number of dispersion lengths to be observable. Confirming this in an experiment

is clearly a considerable challenge. R_1 -symmetric solitons with higher numbers of humps as well as solitons without R_1 symmetry, on the other hand, appear to be much more unstable and break up quite early; hence, they are unlikely to be observable experimentally. Note that Figs. 9 and 10 suggest that the different initial profiles may break up differently, by their pulses interacting in different ways. The further study of such instabilities via the repulsion and/or attraction of neighboring pulse is a challenging subject for future research.

VIII. CONCLUSIONS

We investigated the existence of solitons of the GNLSE in the presence of both quartic and quadratic dispersion terms. Taking a dynamical system approach, we made a traveling wave ansatz to translate solitons of the GNLSE into homoclinic solutions to the equilibrium $\mathbf{0}$ of system (5), which is Hamiltonian and features two reversible symmetries R_1 and R_2 . We found that for both signs of the quadratic dispersion β_2 there exist infinitely many homoclinic solutions of system (5) with different symmetry properties, which correspond to infinitely many solitons of the GNLSE. Each family of homoclinic solutions is associated with a heteroclinic cycle formed by different EtoP connections between $\mathbf{0}$ and a specific periodic solution in the zero-energy level. The symmetries of the periodic solution determine what families of homoclinic solutions they generate.

We presented here four different families of homoclinic solutions, namely, those with R_1 and R_2 symmetry, as well as related R_1 -symmetry-broken and R_2 -symmetry-broken homoclinic solutions. Both the R_1 -symmetric and R_2 -symmetric primary homoclinic solutions emerge from a Hamiltonian-Hopf bifurcation and exist over the entire β_2 interval where $\mathbf{0}$ has complex-conjugate eigenvalues with nonzero real part. All the other R_1 - and R_2 -symmetric and associated symmetry-broken multihump homoclinic solutions, on the other hand, come as pairs on branches that meet at fold points for particular values of β_2 ; the respective fold points accumulate on the β_2 values of folds of the corresponding heteroclinic EtoP connections between $\mathbf{0}$ and periodic solutions in the zero-energy level.

These results were obtained by combining the theory of four-dimensional reversible Hamiltonian system with state-of-the-art continuation techniques that enabled us to compute branches of homoclinic solutions, as well as those of the corresponding EtoP connections that organize them. In this way, we provided numerical evidence for the overall organization of homoclinic solutions, which all emerge or disappear in a Belyakov-Devaney (BD) bifurcation, leading to a structure, also reported in the LL equation [17], that we refer to as BD-truncated homoclinic snaking. We also showed that there exist infinitely many periodic solutions that generate EtoP connections and, hence, associated families of multihump

homoclinic solutions; moreover, we presented the regions of existence of all these different solitons in the (β_2, β_4) and the (β_2, μ) planes. Overall, our results provide guidance in the form of a “road map” of the plethora of solitons exhibited by the GNLSE, and how they are organized in families by EtoP cycles.

Finally, in a first consideration of the stability properties of the various multihump solitons, we checked how far along the fiber a specific perturbation of such a soliton propagates before breaking up. Our simulation results indicate that all solitons, except the R_1 -symmetric single-pulse soliton, are unstable; moreover, the R_1 -symmetric double-hump soliton and the R_1 -symmetric triple-hump soliton appear to be only weakly unstable: (after perturbation) they can be propagated by numerical simulation of the GNLSE over a considerable number of dispersion lengths. Hence, when launched carefully into the right kind of wave guide, they might be observable experimentally. Sustaining such weakly unstable solitons over sufficiently large distances in an experiment is indeed a considerable challenge.

A number of interesting theoretical questions arise from our study. First of all, we have observed that, as β_2 is varied, different surfaces of periodic orbits may interact and bifurcate, which leads to changes of the types of periodic orbits that can be found in the zero-energy level. In turn, this influences the structure of available EtoP connections that organize families of homoclinic orbits. Moreover, we have evidence that connections between the same and/or between different periodic orbits, referred to as PtoP cycles, exist in the zero-energy surface. Hence, more complicated heteroclinic cycles from $\mathbf{0}$ back to itself can be constructed, which presumably generate associated families of homoclinic solutions. The study of these additional connections and associated types of solitons of the GNLSE is the subject of ongoing work. The stability analysis of the different multihump solitons as solutions of the GNLSE, that is, of the PDE, remains a considerable challenge for future work. This will require state-of-the-art techniques, such as the computation of Evans functions [45], because the solitons we found are not bound states of two or more primary solitons. A subsequent study of possible interactions between quartic solitons of different types, and whether they may support bound states or molecules of solitons, also remains an interesting question for future research. Finally, recent experiments [46] have shown the feasibilities of creating waveguides with higher even-order dispersion, such as sextic (β_6), octic (β_8), or decic (β_{10}) dispersion. Our analysis constitutes the first step towards understanding the existence of solitons for different configuration of such higher-order dispersion terms.

ACKNOWLEDGMENT

We would like to thank C. Martijn De Sterke and K. Tam for several helpful discussions.

[1] A. Blanco-Redondo, C. M. De Sterke, J. E. Sipe, T. F. Krauss, B. J. Eggleton, and C. Husko, Pure-quartic solitons, *Nat. Commun.* **7**, 10427 (2016).

[2] K. K. K. Tam, T. J. Alexander, A. Blanco-Redondo, and C. M. De Sterke, Solitary wave solutions in nonlinear media with quartic and quadratic dispersion-implications for high-power

- lasers, *OSA Technical Digest* (Optical Society of America, 2018), paper JW4A.78.
- [3] K. K. K. Tam, T. J. Alexander, A. Blanco-Redondo, and C. M. De Sterke, Stationary and dynamical properties of pure-quartic solitons, *Opt. Lett.* **44**, 3306 (2019).
- [4] K. K. K. Tam, T. J. Alexander, A. Blanco-Redondo, and C. M. De Sterke, Generalized dispersion Kerr solitons, *Phys. Rev. A* **101**, 043822 (2020).
- [5] M. Karlsson and A. Höök, Soliton-like pulses governed by fourth order dispersion in optical fibers, *Opt. Commun.* **104**, 303 (1994).
- [6] M. Piché, J.-F. Cormier, and X. Zhu, Bright optical soliton in the presence of fourth-order dispersion, *Opt. Lett.* **21**, 845 (1996).
- [7] N. N. Akhmediev, A. V. Buryak, and M. Karlsson, Radiationless optical solitons with oscillating tails, *Opt. Commun.* **110**, 540 (1994).
- [8] N. N. Akhmediev and A. V. Buryak, Interactions of solitons with oscillating tails, *Opt. Commun.* **121**, 109 (1995).
- [9] A. V. Buryak and N. N. Akhmediev, Stability criterion for stationary bound states of solitons with radiationless oscillating tails, *Phys. Rev. E* **51**, 3572 (1995).
- [10] S. Roy and F. Biancalana, Formation of quartic solitons and a localized continuum in silicon-based slot waveguides, *Phys. Rev. A* **87**, 025801 (2013).
- [11] A. Boudjemâa and U. Al Khawaja, Stability of n -soliton molecules in dispersion-managed optical fibers, *Phys. Rev. A* **88**, 045801 (2013).
- [12] A. Boudjemâa, Many-soliton bound states in dispersion-managed optical fiber: Possibility of fiber-optic transmission of three bits per clock period, *Int. J. Mod. Phys. B* **31**, 1750178 (2017).
- [13] Y. Kominis and K. T. Hizanidis, Power dependent soliton location and stability in complex photonic structures, *Opt. Express* **16**, 12124 (2008).
- [14] Y. Kominis, Bright, dark, antidark, and kink solitons in media with periodically alternating sign of nonlinearity, *Phys. Rev. A* **87**, 063849 (2013).
- [15] K. Dragonas and Y. Kominis, Solitary wave formation under the interplay between spatial inhomogeneity and nonlocality, *Phys. Rev. E* **100**, 052209 (2019).
- [16] Y. Kominis, J. Cuevas-Maraver, P. G. Kevrekidis, D. J. Frantzeskakis, and A. Bountis, Continuous families of solitary waves in non-symmetric complex potentials: A Melnikov theory approach, *Chaos, Solitons Fractals* **118**, 222 (2019).
- [17] P. Parra-Rivas, D. Gomila, L. Gelens, and E. Knobloch, Bifurcation structure of localized states in the Lugiato-Lefever equation with anomalous dispersion, *Phys. Rev. E* **97**, 042204 (2018).
- [18] J. Burke and E. Knobloch, Snakes and ladders: Localized states in the Swift-Hohenberg equation, *Phys. Lett. A* **360**, 681 (2007).
- [19] P. L. Christiansen, M. P. Sørensen, and A. C. Scott (eds.), *Nonlinear Fiber Optics*, in *Nonlinear Science at the Dawn of the 21st Century* (Springer, Berlin, 2000).
- [20] A. R. Champneys and A. Spence, Hunting for homoclinic orbits in reversible systems: a shooting technique, *Adv. Comput. Math.* **1**, 81 (1993).
- [21] A. R. Champneys, Homoclinic orbits in reversible systems and their applications in mechanics, fluids and optics, *Physica D (Amsterdam)* **112**, 158 (1998).
- [22] R. L. Devaney, Reversible diffeomorphisms and flows, *Trans. Am. Math. Soc.* **218**, 89 (1976).
- [23] R. L. Devaney, Blue sky catastrophes in reversible and Hamiltonian systems, *Indiana Univ. Math. J.* **26**, 247 (1977).
- [24] C. J. Amick and J. F. Toland, Homoclinic orbits in the dynamic phase-space analogy of an elastic strut, *Eur. J. Appl. Math.* **3**, 97 (1992).
- [25] A. R. Champneys and J. F. Toland, Bifurcation of a plethora of multi-modal homoclinic orbits for autonomous Hamiltonian systems, *Nonlinearity* **6**, 665 (1993).
- [26] A. J. Homburg and B. Sandstede, Homoclinic and heteroclinic bifurcations in vector fields, in *Handbook of Dynamical Systems*, Volume 3, edited by H. W. Broer, B. Hasselblatt, and F. Takens (Elsevier, Amsterdam, 2010), pp. 379–524.
- [27] A. J. Elvin, C. R. Laing, R. I. McLachlan, and M. G. Roberts, Exploiting the Hamiltonian structure of a neural field model, *Physica D (Amsterdam)* **239**, 537 (2010).
- [28] M. Haragus and G. Iooss, *Local Bifurcations, Center Manifolds, and Normal Forms in Infinite-Dimensional Dynamical Systems* (Springer, New York, 2010).
- [29] G. Iooss and M. C. Pérouème, Perturbed homoclinic solutions in reversible 1:1 resonance vector fields, *J. Differ. Equ.* **102**, 62 (1993).
- [30] E. J. Doedel and B. E. Oldeman, AUTO-07p: Continuation and Bifurcation Software for Ordinary Differential Equations, Department of Computer Science, Concordia University, Montreal, Canada, 2010, with major contributions from A. R. Champneys, F. Dercole, T. F. Fairgrieve, Y. Kuznetsov, R. C. Paffenroth, B. Sandstede, X. J. Wang, and C. H. Zhang, available at <http://www.cmv1.cs.concordia.ca/>.
- [31] A. R. Champneys, Y. A. Kuznetsov, and B. Sandstede, A numerical toolbox for homoclinic bifurcation analysis, *Int. J. Bifur. Chaos Appl. Sci. Eng.* **6**, 867 (1996).
- [32] B. Krauskopf, H. M. Osinga, and J. Galán-Vioque, *Numerical Continuation Methods for Dynamical Systems* (Springer, Berlin, 2007).
- [33] J. Galan-Vioque, F. J. M. Almaraz, and E. F. Macías, Continuation of periodic orbits in symmetric Hamiltonian and conservative systems, *Eur. Phys. J. Top.* **223**, 2705 (2014).
- [34] E. J. Doedel, R. Paffenroth, H. B. Keller, D. Dichmann, J. Galán, and A. Vanderbauwhede, Continuation of periodic solutions in conservative systems with application to the 3-body problem, *Int. J. Bifur. Chaos Appl.* **13**, 1 (2003).
- [35] F. J. Muñoz Almaraz, E. Freire, J. Galán, E. Doedel, and A. Vanderbauwhede, Continuation of periodic orbits in conservative and Hamiltonian systems, *Physica D (Amsterdam)* **181**, 1 (2003).
- [36] B. Krauskopf and T. Rieß, A Lin's method approach to finding and continuing heteroclinic connections involving periodic orbits, *Nonlinearity* **21**, 1655 (2008).
- [37] G. W. Hunt, H. M. Bolt, and J. M. T. Thompson, Structural localization phenomena and the dynamical phase-space analogy, *Proc. R. Soc. London A* **425**, 245 (1989).
- [38] J. J. Palis and W. De Melo, *Geometric Theory of Dynamical Systems: An Introduction* (Springer, New York, 2012).
- [39] A. R. Champneys, Homoclinic orbits in reversible systems II: Multi-bumps and saddle-centres, *CWI Quarterly* **12**, 185 (1999).
- [40] J. P. England, B. Krauskopf, and H. M. Osinga, Computing one-dimensional global manifolds of Poincaré maps by continuation, *SIAM J. Appl. Dyn. Syst.* **4**, 1008 (2005).

- [41] S. Wiggins and D. S. Mazel, *Introduction to Applied Nonlinear Dynamical Systems and Chaos*, Volume 2 (Springer, New York, 2003).
- [42] P. D. Woods and A. R. Champneys, Heteroclinic tangles and homoclinic snaking in the unfolding of a degenerate reversible Hamiltonian–Hopf bifurcation, *Physica D (Amsterdam)* **129**, 147 (1999).
- [43] A. J. Homburg and J. Knobloch, Multiple homoclinic orbits in conservative and reversible systems, *Trans. Am. Math. Soc.* **358**, 1715 (2006).
- [44] B. Sandstede, Stability of travelling waves, in *Handbook of Dynamical Systems, Volume 2* (Elsevier, Amsterdam, 2002), pp. 983–1055.
- [45] B. Barker, J. Humpherys, G. Lyng, and J. Lytle, Evans function computation for the stability of travelling waves, *Philos. Trans. R. Soc. A* **376**, 20170184 (2018).
- [46] A. F. J. Runge, Y. L. Qiang, T. J. Alexander, M. Z. Rafat, D. D. Hudson, A. Blanco-Redondo, and C. M. de Sterke, Infinite hierarchy of solitons: Interaction of Kerr nonlinearity with even orders of dispersion, *Phys. Rev. Research* **3**, 013166 (2021).